A Self-Oscillation WPT System With High Misalignment Tolerance

Zhihao Wei, Bo Zhang, *Fellow, IEEE*, Shan Lin, and Chunfang Wang, *Member, IEEE*

***Abstract*—High misalignment tolerance is vital in the application of wireless power transfer (WPT) system. In this article, a self-oscillation WPT system with high misalignment tolerance is presented. Under the condition that the compensation equation is satisfied and the input impedance is pure resistance, the output of the S/PS topology WPT system is independent of the coupling coefficient. This article adopts the self-oscillation control method to ensure that the input impedance is pure resistance, so that the fluctuation of the system output is small with the change of the coupling coefficient. Moreover, a parametric design method that can satisfy the design requirements of transmission distance, misalignment, and output voltage is proposed. To deduce the analytical solution of the proposed WPT system, an equivalent coupled-mode method is presented in this article. Finally, the experimental results indicate that when the distance is 20.0 cm and the misalignment is less than 14.9 cm, the output voltage and efficiency of the system remain almost unchanged.**

***Index Terms*—Coupling coefficient, high misalignment tolerance, self-oscillation, wireless power transfer (WPT).**

NOMENCLATURE

L_t	Inductance of the transmitting coil.
L_r	Inductance of the receiving coil.
C_t	Compensation capacitance on the transmitting side.
C_r	Series compensation capacitance on the receiving side.
C_1	Parallel compensation capacitance on the receiving side.
M_{tr}	Mutual inductance.
ω	Working angular frequency.
R_t	Equivalent series resistance of the transmitting coil.
R_r	Equivalent series resistance of the receiving coil.
$-R_N$	Negative resistance.
R_L	Equivalent ac load resistance.
R_o	DC load resistance.
I_t	Current through the transmitting coil.
I_r	Current through the receiving coil.
I_L	Current through the equivalent ac load resistance.
$Z_{\rm in}$	Input impedance.
$U_{\rm in}$	Output voltage of the inverter.
U_L	Equivalent ac output voltage.
η	Transmission efficiency.
$P_{\rm o}$	Output power.
f	Working frequency.
k	Coupling coefficient.
k_c	Critical coupling coefficient.
$k_{\rm min}$	Minimum coupling coefficient for system operation.
f_W	Working frequency in the weak coupling region.
f_H	High frequency.
f_M	Medium frequency.
f_L	Low frequency.
f_d	Detected frequency.
ω_H	Working angular frequency corresponding to $f_{\rm H}$.
ω_L	Working angular frequency corresponding to $f_{\rm L}$.
$G(s)$	Transfer function of inverter output current to inverter output voltage.
U_{LH}	AC output voltage corresponding to $f_{\rm H}$.
U_{LM}	AC output voltage corresponding to $f_{\rm M}$.
U_{LL}	AC output voltage corresponding to $f_{\rm L}$.
η_H	Transmission efficiency corresponding to $f_{\rm H}$.
η_M	Transmission efficiency corresponding to $f_{\rm M}$.
η_L	Transmission efficiency corresponding to $f_{\rm L}$.
γ	Ratio of C_1 to $C_{\rm r}$.
D_r	Diameter of the coil.
μ_0	Vacuum permeability.
K_N	Coefficient of space spiral coil.
N	Number of turns of the coil.
h	Height of the coil.
D_1	Diameter of the wire.
p_1	Turn pitch.
$R_{L\rm eq}$	Equivalent resistance of the receiving side circuit.
$C_{r\rm eq}$	Equivalent capacitance of the receiving side circuit.
a_t	Energy mode of the transmitting side circuit.
a_r	Energy mode of the receiving side circuit.
A_t	Amplitude of the energy mode of the transmitting side circuit.
A_r	Amplitude of the energy mode of the receiving side circuit.
θ_t	Phase of the energy mode of the transmitting side circuit.
θ_r	Phase of the energy mode of the receiving side circuit.

Manuscript received 29 May 2023; revised 1 September 2023 and 18 October 2023; accepted 20 October 2023. Date of publication 24 October 2023; date of current version 6 December 2023. This work was supported in part by the National Natural Science Foundation of China under Grant 51877113, in part by the Shandong Youth Innovation Team under Grant 2022KJ150, and in part by the Youth Project of Natural Science Foundation of Shandong Province under Grant ZR2023QE298. Recommended for publication by Associate Editor C. Tse. *(Corresponding author: Chunfang Wang.)*

Zhihao Wei and Chunfang Wang are with the School of Electrical Engineering, Qingdao University, Qingdao 266071, China (e-mail: epweizh@qdu.edu.cn; qduwcf@qdu.edu.cn).

Bo Zhang is with the School of Electric Power Engineering, South China University of Technology, Guangzhou 510641, China (e-mail: epbzhang@scut.edu.cn).

Shan Lin is with the Guangzhou Metro Design and Research Institute, Guangzhou 510010, China (e-mail: linshan1@gmdi.cn).

Color versions of one or more figures in this article are available at https://doi.org/10.1109/TPEL.2023.3327096.

Digital Object Identifier 10.1109/TPEL.2023.3327096

ω_t Natural resonance angular frequency of the transmitting side circuit.
ω_r Natural resonance angular frequency of the receiving side circuit.
g_t Total gain rate of the transmitting side circuit.
τ_r Total loss rate of the receiving side circuit.
τ_{tt} Inherent loss rate of transmitting side circuit.
κ Coupling rate.
U_o DC output voltage.
$U_{o\text{set}}$ Design value of output voltage.
V_{DC} DC input voltage.
d Transmission distance.

I. Introduction

WIRELESS power transfer (WPT) system has extensive application prospects in autonomous underwater vehicles [1], [2], [3], [4], electric vehicles [5], [6], [7], [8], [9], implantable devices [10], [11], [12], [13], automatic guided vehicles [14], [15], [16], [17], [18], [19], electric bicycles [20], [21], [22], and other occasions. However, coil misalignment is inevitable in these applications. For instance, it is difficult for the driver to park the electric vehicle at the charging point accurately, and its coils will be misaligned. In addition, due to the presence of waves, the relative position between the coils in the autonomous underwater vehicles constantly varies, which causes the coils to always fail to align. The output voltage and efficiency of the WPT system are generally sensitive to misalignment, that is, when the coils are misaligned, the output voltage and efficiency of the system will change [23], [24]. The weak spatial freedom will limit the development of WPT technology.

In order to improve the misalignment tolerance of the system, there are mainly the following methods.

1) Optimizing the structure of the magnetic coupler [25], [26], [27]. This method improves misalignment tolerance by reducing the change in mutual inductance when coils are misaligned. A split flat solenoid coupler is presented in [25], and the magnetic coupler heightens the lateral misalignment tolerance. Besides, this literature proposes an optimization approach for the split flat solenoid coupler to achieve a good balance between misalignment tolerance, cost, and coupling. In [26], a magnetic coupler with series double D pads and solenoid is presented. The coupler not only enhances the lateral misalignment tolerance, but also improves the longitudinal misalignment tolerance. Zhao et al. [27] propose a family of hybrid WPT magnetic coupler, which combines a BP coupler and an S/S topology to achieve an equivalent coupling coefficient with a small variation tendency, thus realizing high misalignment tolerance. This method has misalignment tolerance only in some directions, not all directions. Moreover, the output and efficiency of this method fluctuate significantly when the coil is offset.
2) Optimizing system parameters [28], [29], [30], [31]. Mai et al. [28], Wang et al. [29], and Zhu et al. [30] propose a method for designing system parameters with high misalignment tolerance, and this method designs the system to work near the extreme point. When the coupling coefficient changes near the extreme point, the system output fluctuates less, thus improving the misalignment tolerance. Wang et al. [29] also points out that if the parameters of the compensation circuit are properly designed, all compensation topologies with parallel compensation components on the receiving side have a strong misalignment tolerance capability. A method for optimizing the compensation capacitor is proposed in [31], which improves the impedance characteristics and thus enhances the lateral misalignment tolerance. The output and efficiency of this method fluctuate greatly when the coil is offset. Besides, this method will introduce a large amount of reactive power and reduce the efficiency of the system.
3) Novel topological structures [32], [33], [34], [35]. A series hybrid topology is proposed in [34]. When the coil is offset, the output characteristics of the two topologies are opposite, thereby reducing output fluctuations and enhancing misalignment tolerance. Qu et al. [35] propose a WPT system with dual coupling inductor-capacitor-capacitor and series compensation. The main coil and the compensation coil are integrated as two decoupling coils, while they are both coupled with the receiving coil. When the coil is offset, the two mutual inductances between the two decoupling coils on the transmitting side and the receiving coil have opposite effects on the output power, so that the output power remains basically stable. This method requires many passive components, which increases the cost of the system. In addition, the system cannot implement zero phase angle (ZPA).
4) PT-symmetry principle [36]. When the system remains unchanged under the joint parity and time reversal operations, the system is PT-symmetry. The output and efficiency of the PT-symmetric WPT system in the PT-symmetric region are independent of the coupling coefficient, and it has a strong misalignment tolerance capability. However, only a few topological WPT systems are PT-symmetry.

The self-oscillation control strategy can achieve better dynamic response and adaptability and has attracted more and more attention. Wu et al. [37] proposed a self-oscillation controller based on pulse width modulator. The switching frequencies of the transmitting side inverter and the receiving side rectifier could be synchronized with the resonant currents of the transmitting side and the receiving side, respectively, so as to realize the self-oscillation control with tolerance and fast response to the compensation parameter error. Yan et al. [38] proposed a self-oscillation control strategy for series–series type WPT system. By detecting the current phase of the receiving side to control the inverter on the transmitting side, better output controllability, dynamic response, and adaptability can be achieved. Ren et al. [39] proposed a self-oscillation WPT system with a delay in the feedback loop on the transmitting side and proposed a delay iteration method for self-tuning of the self-oscillation frequency. The disturbance observation method can be used

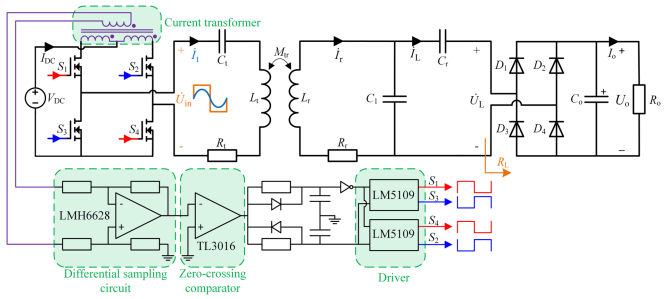

Fig. 1. Circuit diagram of the proposed WPT system.

to tune the system parameters with an adjustable capacitor on the transmitting side while the frequency is self-tuning, and the synchronous tuning method here is stable and accurate.

Therefore, to address the abovementioned problems and enhance the misalignment tolerance, this work proposes a self-oscillation WPT system with S/PS compensation topology. The output voltage and efficiency of the proposed system in the strong coupling region are insensitive to the coupling coefficient. Therefore, the proposed system has a high misalignment tolerance in all directions. Furthermore, the proposed system uses the self-oscillation control method to achieve negative resistance, and the system has a unity power factor and high system efficiency. Simultaneously, the proposed system has a simple topology, requires fewer passive components, and has a low cost.

The main contributions of this article are as follows.

1) A self-oscillation WPT system with high misalignment tolerance is presented. The output voltage and efficiency of the S/PS topology WPT system in the strong coupling region are not sensitive to the coupling coefficient under the condition that the compensation equation is satisfied and the input impedance is pure resistance. Besides, a parameter design method is proposed, which can meet the design requirements of transmission distance, misalignment, and output voltage.
2) The traditional coupled-mode method can only model and analyze the first-order compensation topology WPT system. This article proposes an equivalent coupled-mode method that can establish the model of the higher-order compensation topology WPT system.

The rest of this article is organized as follows. In Section II, the self-oscillation WPT system is modeled and analyzed. In Section III, an equivalent coupled-mode method is proposed to obtain the analytical solution of the S/PS compensation topology WPT system. The theoretical results are evaluated experimentally in Section IV. Finally, Section V concludes this article.

II. Analysis of the Proposed System

A. System Model

The circuit diagram of the proposed WPT system is illustrated in Fig. 1. The self-oscillation control method is adopted in the proposed system. The output voltage and output current of the inverter have the same phase, and the inverter is equivalent to the negative resistance. Hence, the system can be represented by the following equation:

$$\begin{bmatrix} -R_N + R_t + \frac{1}{j\omega C_t} + j\omega L_t & j\omega M_{tr} & 0 \\ j\omega M_{tr} & j\omega L_r + R_r & \frac{1}{j\omega C_r} + R_L \\ 0 & -\frac{1}{j\omega C_1} & \frac{1}{j\omega C_1} + \frac{1}{j\omega C_r} + R_L \end{bmatrix} \times \begin{bmatrix} \dot{I}_t \\ \dot{I}_r \\ \dot{I}_L \end{bmatrix} = \begin{bmatrix} 0 \\ 0 \\ 0 \end{bmatrix}. \quad (1)$$

Here, L_t and L_r represent the transmitting coil and the receiving coil respectively. C_t, C_r, and C_1 are compensation capacitors. They satisfy the compensation equation $1/\sqrt{L_t C_t} = 1/\sqrt{L_r(C_r + C_1)}$. R_t and R_r are the equivalent series resistances of the transmitting coil and the receiving coil, respectively. M_{tr} indicates the mutual inductance, and ω represents the working angular frequency. $-R_{\mathrm{N}}$ and R_L are the negative resistance and the equivalent ac load resistance respectively. $\dot{I}_t$, $\dot{I}_r$, and $\dot{I}_L$ indicate the current through the transmitting coil, the current through the receiving coil, and the current through the equivalent ac load resistance, respectively.

From (1), the ratio of the system output current to the inverter output current can be deduced

$$\frac{I_L}{I_t} = \frac{M_{tr}}{C_1\sqrt{X_1}} \quad (2)$$

where $X_1 = (L_r/C_1 + L_r/C_r + R_r R_L - 1/\omega^2 C_r C_1)^2 + [-R_r/\omega C_r + \omega L_r R_L - (R_r + R_L)/\omega C_1]^2$.

The input impedance of the system is as follows:

$$Z_{\mathrm{in}} = R_t + j\omega L_t + \frac{1}{j\omega C_t} + \frac{\omega^2 M_{tr}^2}{R_r + j\omega L_r + \left(\frac{1}{j\omega C_r} + R_L // \frac{1}{j\omega C_1}\right)}. \quad (3)$$

When the system adopts the self-oscillation control method, the imaginary part of the input impedance is zero. At this time, the following equation can be derived from (3):

$$\left(\omega L_t - \frac{1}{\omega C_t}\right) - \frac{\omega^2 M_{tr}^2 (\omega L_r - X_3)}{(R_r + X_2)^2 + (\omega L_r - X_3)^2} = 0. \quad (4)$$

Here, $X_2 = R_L C_r^2/[\omega^2 C_r^2 C_1^2 R_L^2 + (C_r + C_1)^2]$ and $X_3 = (C_r + C_1 + \omega^2 C_1 C_r^2 R_L^2)/[\omega^3 C_r^2 C_1^2 R_{\mathrm{L}}^2 + \omega(C_r + C_1)^2]$.

On the basis of (3), the negative resistance can be expressed as

$$-R_N = -R_t - \frac{(R_r + X_2)\left(\omega^2 L_t C_t - 1\right)}{\omega^2 L_r C_t - \omega C_t X_3}. \quad (5)$$

The output current of the inverter can be described as

$$I_{\mathrm{t}} = \frac{U_{\mathrm{in}}}{R_t + \frac{(R_r + X_2)(\omega^2 L_t C_t - 1)}{\omega^2 L_r C_t - \omega C_t X_3}} \quad (6)$$

where U_{in} is the output voltage of the inverter.

Based on (2), (4), and (6), the output current of the system can be derived, and then the equivalent ac output voltage of the

TABLE I
COMPARISON OF THE TRANSMISSION CHARACTERISTICS OF FOUR SELF-OSCILLATION WPT SYSTEMS WITH BASIC TOPOLOGIES

Topology	Conditions	Critical coupling coefficient	Output Power	Efficiency
S/S	$\begin{cases} \mathrm{Im}(Z_{\mathrm{in}})=0 \\ \frac{1}{\sqrt{L_{\mathrm{t}}C_{\mathrm{t}}}}=\frac{1}{\sqrt{L_{\mathrm{r}}C_{\mathrm{r}}}} \end{cases}$	$k_{\mathrm{c}}=\frac{R_{\mathrm{r}}+R_{\mathrm{L}}}{\omega_{\mathrm{t}}L_{\mathrm{r}}}$	$P_{\mathrm{o}}=\frac{4L_{\mathrm{t}}^2L_{\mathrm{r}}G_0^2R_{\mathrm{L}}}{\left[R_{\mathrm{t}}L_{\mathrm{r}}+\left(R_{\mathrm{r}}+R_{\mathrm{L}}\right)L_{\mathrm{t}}\right]^2}$	$\eta=\frac{R_{\mathrm{L}}L_{\mathrm{t}}}{L_{\mathrm{t}}R_{\mathrm{t}}+\left(R_{\mathrm{r}}+R_{\mathrm{L}}\right)L_{\mathrm{t}}}$
S/P	$\begin{cases} \mathrm{Im}(Z_{\mathrm{in}})=0 \\ \frac{1}{\sqrt{L_{\mathrm{t}}C_{\mathrm{t}}}}=\frac{1}{\sqrt{L_{\mathrm{r}}C_{\mathrm{r}}}} \end{cases}$	$k_{\mathrm{c}}=\frac{R_{\mathrm{r}}}{\omega_{\mathrm{t}}L_{\mathrm{r}}}+\frac{\omega_{\mathrm{t}}L_{\mathrm{r}}}{R_{\mathrm{L}}}$	$P_{\mathrm{o}}=\frac{4L_{\mathrm{t}}^2L_{\mathrm{r}}^2C_{\mathrm{r}}G_0^2R_{\mathrm{L}}}{\left[R_{\mathrm{L}}R_{\mathrm{t}}L_{\mathrm{r}}C_{\mathrm{r}}+R_{\mathrm{L}}R_{\mathrm{r}}L_{\mathrm{t}}C_{\mathrm{r}}+L_{\mathrm{t}}L_{\mathrm{r}}\right]^2}$	$\eta=\frac{1}{\frac{R_{\mathrm{t}}R_{\mathrm{L}}}{\omega_{\mathrm{t}}^2L_{\mathrm{t}}L_{\mathrm{r}}}+\frac{R_{\mathrm{r}}R_{\mathrm{L}}}{\omega_{\mathrm{t}}^2L_{\mathrm{r}}^2}+1}$
P/S	$\begin{cases} \mathrm{Im}(Z_{\mathrm{in}})=0 \\ \frac{1}{\sqrt{L_{\mathrm{t}}C_{\mathrm{t}}}}=\frac{1}{\sqrt{L_{\mathrm{r}}C_{\mathrm{r}}}} \end{cases}$	$k_{\mathrm{c}}=\frac{R_{\mathrm{r}}+R_{\mathrm{L}}}{\omega_{\mathrm{t}}L_{\mathrm{r}}}$	$P_{\mathrm{o}}=\frac{4G^2L_{\mathrm{t}}^2R_{\mathrm{L}}L_{\mathrm{r}}}{\left[R_{\mathrm{t}}L_{\mathrm{r}}+\left(R_{\mathrm{r}}+R_{\mathrm{L}}\right)L_{\mathrm{t}}\right]^2}$	$\eta=\frac{R_{\mathrm{L}}L_{\mathrm{t}}}{L_{\mathrm{r}}R_{\mathrm{t}}+\left(R_{\mathrm{r}}+R_{\mathrm{L}}\right)L_{\mathrm{t}}}$
P/P	$\begin{cases} \mathrm{Im}(Z_{\mathrm{in}})=0 \\ \frac{1}{\sqrt{L_{\mathrm{t}}C_{\mathrm{t}}}}=\frac{1}{\sqrt{L_{\mathrm{r}}C_{\mathrm{r}}}} \end{cases}$	$k_{\mathrm{c}}=\frac{R_{\mathrm{r}}}{\omega_{\mathrm{t}}L_{\mathrm{r}}}+\frac{\omega_{\mathrm{t}}L_{\mathrm{r}}}{R_{\mathrm{L}}}$	$P_{\mathrm{o}}=\frac{4G^2L_{\mathrm{t}}^2L_{\mathrm{r}}^2R_{\mathrm{L}}C_{\mathrm{r}}}{\left[R_{\mathrm{L}}R_{\mathrm{t}}L_{\mathrm{r}}C_{\mathrm{r}}+R_{\mathrm{L}}R_{\mathrm{r}}L_{\mathrm{t}}C_{\mathrm{r}}+L_{\mathrm{t}}L_{\mathrm{r}}\right]^2}$	$\eta=\frac{1}{\frac{R_{\mathrm{t}}R_{\mathrm{L}}}{\omega_{\mathrm{t}}^2L_{\mathrm{t}}L_{\mathrm{r}}}+\frac{R_{\mathrm{r}}R_{\mathrm{L}}}{\omega_{\mathrm{t}}^2L_{\mathrm{r}}^2}+1}$

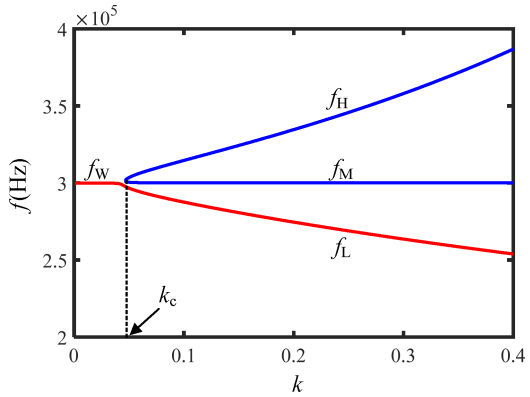

Fig. 2. Curve of the working frequency versus the coupling coefficient.

TABLE II
EXPERIMENTAL PARAMETERS OF THE PROPOSED SYSTEM

Symbol	Note	Values
V_{DC}	Input voltage	48 V
L_{t}	Transmitting coil	70 μH
L_{r}	Receiving coil	70 μH
R_{t}	Internal resistance of transmitting coil	0.25 Ω
R_{r}	Internal resistance of receiving coil	0.25 Ω
C_{t}	Compensation capacitor	4.02 nF
C_{r}	Compensation capacitor	3.01 nF
C_{l}	Compensation capacitor	1.01 nF
R_{o}	DC load resistance	12.3 Ω

system can be obtained

$$U_L=\frac{U_{\mathrm{in}}R_L\sqrt{\left[(R_r+X_2)^2+(\omega L_r-X_3)^2\right](\omega^2L_tC_t-1)}}{\omega C_1R_{\mathrm{N}}\sqrt{X_1\left[\omega^2L_rC_t-\omega C_tX_3\right]}}. \tag{7}$$

The transmission efficiency of the system can be expressed as

$$\eta=\frac{U_L^2}{I_t^2R_L\left(R_t+\frac{(R_r+X_2)(\omega^2L_tC_t-1)}{\omega^2L_rC_t-\omega C_tX_3}\right)}. \tag{8}$$

The curve of the working frequency f versus the coupling coefficient k can be drawn according to (4), as shown in Fig. 2. The parameters adopted in Fig. 2 are the same as those in Table II. The working frequency is $f=\omega/2\pi$, and the relationship between the coupling coefficient and the mutual inductance is $k=M_{\mathrm{tr}}/\sqrt{L_{\mathrm{t}}L_{\mathrm{r}}}$. It can be observed from Fig. 2 that when the coupling coefficient is less than the critical coupling coefficient k_c (weak coupling region), the working frequency has a real solution as f_W. When the coupling coefficient is greater than the critical coupling coefficient k_c (strong coupling region), the working frequency has three real solutions, namely high frequency f_H, medium frequency f_M, and low frequency f_L, but only the high frequency f_H and low frequency f_L are stable.

B. Stability Analysis

The frequency stability is analyzed by Hamel locus method [39]. The transfer function of inverter output current to inverter output voltage is:

$$G(s)=\frac{I_t(s)}{U_{\mathrm{in}}(s)}=\frac{c_4s^4+c_3s^3+c_2s^2+c_1s}{b_5s^5+b_4s^4+b_3s^3+b_2s^2+b_1s+b_0} \tag{9}$$

where $b_5=R_LL_tL_rC_tC_r^2C_1-M_{tr}^2R_LC_tC_r^2C_1$, $b_4=R_LR_tL_rC_tC_r^2C_1+L_tL_rC_tC_r^2+L_tL_rC_tC_rC_1+R_LR_rL_tC_tC_r^2C_1-M_{tr}^2C_tC_r^2-M_{tr}^2C_tC_rC_1$, $b_3=R_tL_rC_tC_r^2+R_tL_rC_tC_rC_1+R_rL_tC_tC_rC_1+R_LL_rC_r^2C_1+R_rL_tC_tC_r^2+R_LR_tR_rC_tC_r^2C_1+R_LL_tC_tC_r^2$, $b_2=R_tR_rC_tC_r^2+R_LR_rC_r^2C_1+L_tC_tC_r+R_tR_rC_tC_rC_1+R_LR_tC_tC_r^2+L_rC_r^2+L_rC_rC_1$, $b_1=R_tC_tC_r+R_rC_r^2+R_rC_rC_1+R_LC_r^2$, $b_0=C_r$, $c_4=R_LL_rC_tC_r^2C_1$, $c_3=R_LR_rC_tC_r^2C_1+L_rC_tC_r^2+L_rC_tC_rC_1$, $c_2=R_rC_tC_r^2+R_rC_tC_rC_1+R_LC_tC_r^2$, $c_1=C_tC_r$.

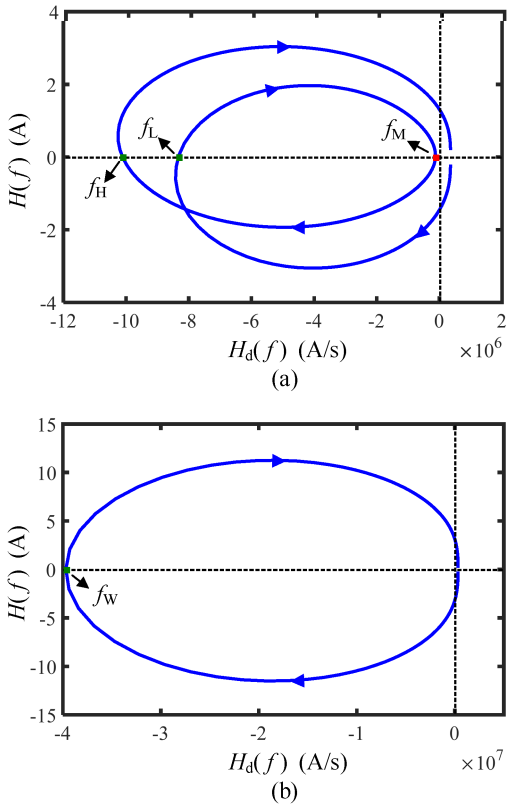

Fig. 3 Hamel locus of the inverter output current. (a) Strong coupling region. (b) Weak coupling region.

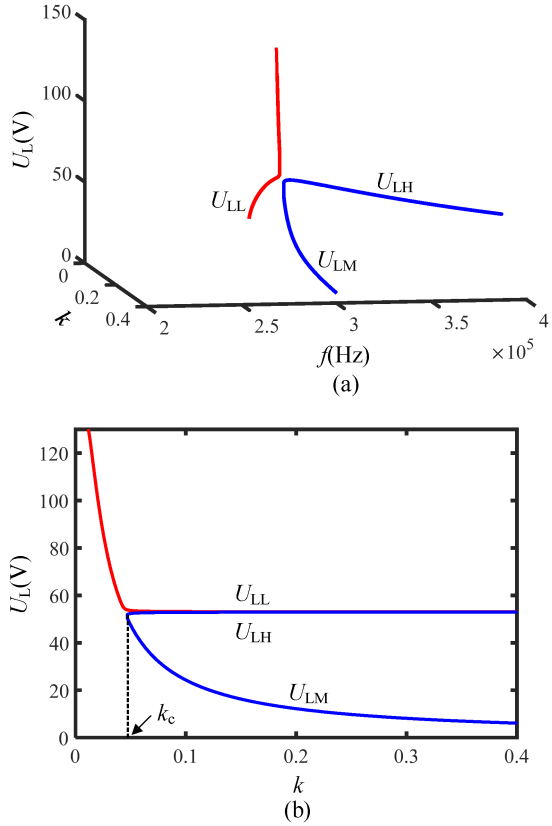

Fig. 4. Output voltage curve of the proposed system. (a) Three-dimensional curve. (b) Side view.

The unit step response of $G(s)$ can be derived by the inverse Laplace transform

$$g(t) = \mathcal{L}^{-1}\left[\frac{G(s)}{s}\right]. \tag{10}$$

The time domain expression of the inverter output current is

$$i_t(t) = \frac{\pi U_{\text{in}}}{2\sqrt{2}}\left[\sum_{n=0}^{\infty} g(t+nT) - \sum_{n=1}^{\infty} g\left(t-\frac{T}{2}+nT\right)\right]. \tag{11}$$

The Hamel locus equation can be described as

$$\begin{cases} H(f) = i_t\left(\frac{1}{2f}\right) \\ H_d(f) = \left.\frac{di_t(t)}{dt}\right|_{t=\frac{1}{2f}} \end{cases}. \tag{12}$$

The Hamel locus of the inverter output current is shown in Fig. 3. Fig. 3(a) describes the Hamel locus of the inverter output current in the strong coupling region, and the coupling coefficient in the figure is 0.2. Other parameters are the same as those in Table II, and the critical coupling coefficient of the system at those parameters is 0.0444. At this time, the system works in the strong coupling region. The direction of the arrow in the figure represents the direction in which the frequency increases. Along the direction of increasing frequency, the trajectory goes through y = 0 from bottom to top, and the intersection with y = 0 is on the negative x-axis, then the intersection, in this case, is stable.

It can be seen from Fig. 3(a) that when the system works in the strong coupling region, there are three intersections between the trajectory and $y = 0$, which correspond to high frequency f_H, medium frequency f_M, and low frequency f_L, respectively. According to the above analysis, the system is stable at f_{H} and f_{L}, and unstable at f_{M}.

The Hamel locus of the inverter output current in the weak coupling region is depicted in Fig. 3(b). The coupling coefficient in the figure is 0.02, and the system operates in the weak coupling region. As can be observed from Fig. 3(b), when the system works in the weak coupling region, there is only one intersection between the trajectory and $y = 0$, which corresponds to frequency f_W, and the system is stable at f_W.

C. Transmission Characteristics

The output voltage curve of the proposed system is described in Fig. 4. Fig. 4(a) is the three-dimensional curve of output voltage, coupling coefficient, and working frequency, and Fig. 4(b) is the side view of the three-dimensional curve. When the coupling coefficient is less than the critical coupling coefficient, the output voltage of the system varies with the coupling coefficient. When the coupling coefficient is greater than the critical coupling coefficient, the output voltage corresponding to high frequency f_H is U_{LH}, the output voltage corresponding to medium frequency f_M is U_{LM}, and the output voltage corresponding to low frequency f_L is U_{LL}. U_{LH} and U_{LL} are stable, and U_{LM}

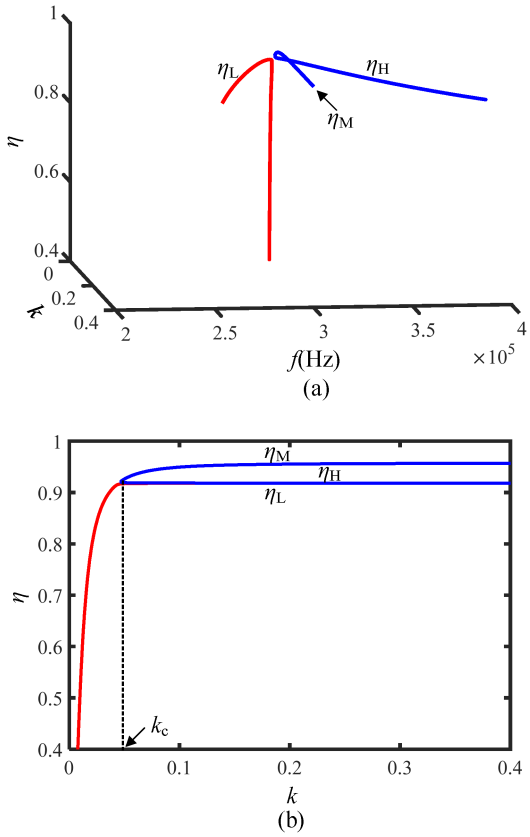

Fig. 5. Efficiency curve of the proposed system. (a) Three-dimensional curve. (b) Side view.

is unstable. The output voltages U_{LH} and U_{LL} of the system in the strong coupling region are basically unchanged with the change of coupling coefficient.

It should be noted that when the coupling coefficient changes, the self-oscillation control circuit will automatically track f_H or f_L in order to always keep the phase of the inverter output voltage the same as that of the inverter output current. At this time, the output voltage of the system in the strong coupling region is insensitive to the coupling coefficient.

Fig. 5 presents the efficiency curve of the proposed system. As can be observed from Fig. 5, when the coupling coefficient is less than the critical coupling coefficient, the system efficiency increases with the increase of the coupling coefficient. When the coupling coefficient is greater than the critical coupling coefficient, the efficiencies η_H and η_L remain basically unchanged with the change of coupling coefficient. Hence, when the distance between the coils is changed or the coils are misaligned, the output voltage and efficiency of the proposed system in the strong coupling region remain basically unchanged, and the proposed system has a high misalignment tolerance.

III. Equivalent Coupled Mode Method and System Design

A. Equivalent Coupled Mode Method

Based on the above analysis, it is difficult to obtain an analytical solution for the S/PS compensation topology by circuit theory. In addition, the traditional coupled-mode method is only used for modeling and analysis of the first-order compensation network, thus the traditional coupled-mode method cannot model the S/PS compensation topology.

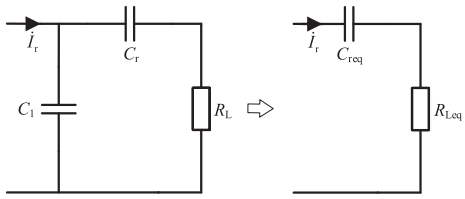

Fig. 6. Equivalent transformation of the receiving side circuit.

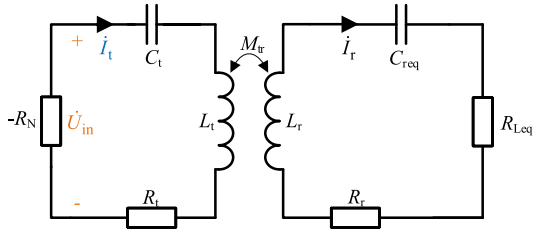

Fig. 7. Equivalent circuit of the proposed WPT system.

To obtain the analytical solution of the proposed WPT system, an equivalent coupled-mode method is proposed in this article. The PS compensation topology on the receiving side is equivalently transformed into the S compensation topology on the receiving side, and then the equivalent S/S compensation topology is modeled and analyzed by the coupled mode theory.

Fig. 6 is a schematic diagram of the equivalent transformation from the PS compensation topology on the receiving side to the S compensation topology on the receiving side, and their parameter relationships are

$$\begin{cases} R_{Leq} = \frac{R_L C_r^2}{(C_r+C_1)^2+(\omega C_r C_1 R_L)^2} \\ C_{req} = \frac{(C_r+C_1)^2+(\omega C_r C_1 R_L)^2}{(C_r+C_1)+\omega^2 C_r^2 C_1 R_L^2} \end{cases}. \tag{13}$$

Since $(C_r + C_1)^2 \gg (\omega C_r C_1 R_L)^2$ and $(C_r + C_1) \gg \omega^2 C_r^2 C_1 R_L^2$, (13) can be simplified as

$$\begin{cases} R_{Leq} = \frac{R_L C_r^2}{(C_r+C_1)^2} \\ C_{req} = C_r + C_1 \end{cases}. \tag{14}$$

The equivalent circuit of the proposed WPT system is shown in Fig. 7. The equivalent circuit is modeled and analyzed by coupled mode theory [40], and Fig. 7 can be described as

$$\frac{d}{dt}\begin{bmatrix} \boldsymbol{a}_t \\ \boldsymbol{a}_r \end{bmatrix} = \begin{bmatrix} j\omega_t + g_t & -j\kappa \\ -j\kappa & j\omega_r - \tau_r \end{bmatrix}\begin{bmatrix} \boldsymbol{a}_t \\ \boldsymbol{a}_r \end{bmatrix}. \tag{15}$$

Here, $a_t = A_t e^{j(\omega t+\theta_t)}$ and $a_r = A_r e^{j(\omega t+\theta_r)}$ are the energy modes of the transmitting and receiving circuits respectively. A_t and A_r are the amplitudes of the energy modes, and θ_t and θ_r are the phases of the energy modes. The natural resonance angular frequencies ω_t and ω_r can be described as:$\omega_t = 1/\sqrt{L_t C_t}$, $\omega_r = 1/\sqrt{L_r C_{\text{req}}}$ respectively, and $\omega_t = \omega_r$. The total gain rate

of the transmitting circuit is $g_t = (G_0/A_t) - \tau_{tt}$, and $G_0 = U_{\text{in}}/2\sqrt{L_t}$. The inherent loss rate of transmitting circuit is $\tau_{tt} = R_t/2L_t$, and the total loss rate of the receiving circuit is $\tau_r = (R_r + R_{Leq})/(R_r + R_{Leq})2L_r2L_r$. The coupling rate of the system is $\kappa = k\omega_t/2$.

According to (15), the characteristic equation of frequency can be obtained.

$$\begin{vmatrix} j(\omega-\omega_t)-g_t & j\kappa \\ j\kappa & j(\omega-\omega_r)+\tau_r \end{vmatrix} = 0. \tag{16}$$

The expression for working angular frequency can be derived from (16)

$$\omega = \omega_t + j\frac{g_t-\tau_r}{2} \pm \sqrt{\kappa^2 - \left(\frac{g_t+\tau_r}{2}\right)^2}. \tag{17}$$

The solution of the working angular frequency can be divided into following two cases.

1) When $\kappa^2 = g_t\tau_r$, the working angular frequency is $\omega = \omega_t$, and the frequency solution is unstable in the strong coupling region according to the Hammel locus method.
2) When $g_t = \tau_r$ and $\kappa > \tau_r$, the working angular frequency is $\omega = \omega_t \pm \sqrt{\kappa^2 - \tau_r^2}$. That is, the analytical expressions of ω_H and ω_L are high frequency $\omega_H = 2\pi f_H = \omega_t + \sqrt{\kappa^2 - \tau_r^2}$ and low frequency $\omega_L = 2\pi f_L = \omega_t - \sqrt{\kappa^2 - \tau_r^2}$. The imaginary part of the input impedance of the system at ω_H and ω_L is zero. For the condition $g_t = \tau_r$, it is necessary to set the nonlinear saturation gain in the system, and the nonlinear saturation gain is usually the negative resistance constructed by the operational amplifier [41]. In this article, to improve the efficiency and power of the system, the negative resistance is realized by the self-oscillation control circuit. For the condition $\kappa > \tau_r$, since $\kappa = k\omega_t/2$ and $\tau_r = (R_r + R_{Leq})/2L_r$, $\kappa > \tau_r$ can be transformed into $k > k_c = (R_r + R_{Leq})/\omega_t L_r$. By limiting the working region, the coupling coefficient of the system can meet the above inequality. Here, k_c is defined as the critical coupling coefficient, and its expression is

$$k_c = \frac{R_r + R_{Leq}}{\omega_t L_r} = \frac{R_L\sqrt{C_r}}{\sqrt{L_r}}\frac{\sqrt{(1+\gamma)}}{(1+\gamma)^2} \tag{18}$$

where γ is denoted as $\gamma = C_1/C_r$. In this article, it is defined that k greater than k_c is the strong coupling region, and k less than k_c is the weak coupling region.

From (15), it can be deduced that the amplitude of the energy mode is

$$|a_t| = |a_r| = \frac{U_{\text{in}}}{2\sqrt{L_t}}\frac{1}{\tau_{tt}+\tau_r}. \tag{19}$$

The output power and transmission efficiency of the system can be expressed as

$$P_{\text{o}} = 2\tau_L|a_r|^2 = \frac{U_{\text{in}}^2 R_{Leq}}{\left[\frac{R_tL_r}{L_t} + R_r + R_{Leq}\right]^2}\frac{L_r}{L_t} \tag{20}$$

$$\eta = \frac{2\tau_L|a_r|^2}{2\tau_{tt}|a_t|^2 + 2\tau_r|a_r|^2} = \frac{R_{Leq}}{\frac{R_tL_r}{L_t} + (R_r + R_{Leq})}. \tag{21}$$

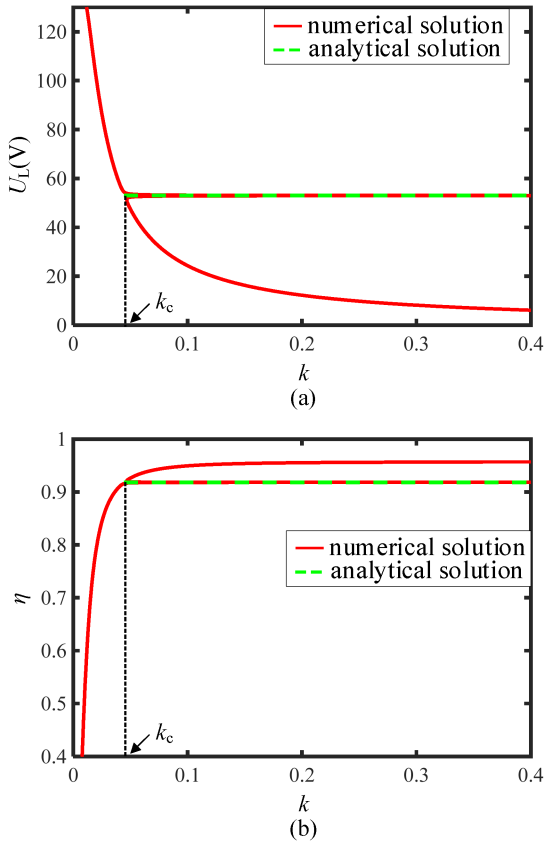

Fig. 8. Comparison between the analytical solution obtained by the equivalent coupled mode method and the numerical solution in Section II.

The analytical expression for the ac output voltages U_L in the strong coupling region is

$$U_L = \frac{U_{\text{in}}\sqrt{R_LR_{Leq}}}{\left[\frac{R_tL_r}{L_t} + R_r + R_{Leq}\right]}\sqrt{\frac{L_r}{L_t}}. \tag{22}$$

From (21) and (22), it can be seen that when the system works in the strong coupling region, the output voltage and efficiency of the system are independent of the coupling coefficient.

The comparison between the analytical solution obtained by the equivalent coupled-mode method and the numerical solution in Section II [see (7) and (8)] is shown in Fig. 8. It can be seen from Fig. 8 that the analytical solution of the output voltage and efficiency is basically consistent with the numerical solution. Therefore, the proposed equivalent coupled-mode method can effectively model and analyze WPT systems with high-order compensation topology.

Furthermore, since the equivalent series resistance R_t and R_r of the coil are much smaller than the equivalent load resistance R_{Leq}, the equivalent series resistance of the coil can be ignored. Equation (22) can be simplified as

$$U_L = \frac{U_{\text{in}}(C_r + C_1)\sqrt{L_r}}{C_r\sqrt{L_t}} = \frac{(1+\gamma)\sqrt{L_r}}{\sqrt{L_t}}U_{\text{in}}. \tag{23}$$

The dc output voltage can be deduced as [42]

$$U_{\mathrm{o}} = \frac{\pi}{2\sqrt{2}} U_L = \frac{\pi}{2\sqrt{2}} \frac{(1+\gamma)\sqrt{L_r}}{\sqrt{L_t}} U_{\mathrm{in}}. \tag{24}$$

From the above equation, it can be seen that in the strong coupling region, the output voltage is independent of the coupling coefficient and load resistance. Therefore, when the load resistance changes, as long as the proposed WPT system operates in the strong coupling region, the output voltage of the system remains basically unchanged with the change of coupling coefficient, that is, the proposed system has antimisalignment tolerance capability.

In addition, the proposed system has inherent constant voltage output characteristics. Consequently, the proposed WPT system can be applied to occasions that require constant voltage power supply, such as heating-type kitchen electrical equipment, wireless power supply for oil drilling, and wireless power supply for high-voltage transmission line monitoring equipment. When the proposed WPT system is applied to kitchen electrical equipment that requires a constant voltage power supply, the output power can be adjusted by the following two methods. 1) Adjust the output power by switching different load resistances. According to (20), the output power is related to the load resistance. Therefore, when the system switches different load resistances, the output power changes. 2) Adjust the output power by changing the ratio of rated output power time to zero output power time. When $0 < t < DT$, the driver is enabled, the driver outputs the control signal, and the system outputs the rated power. When $DT < t < T$, the driver is disabled, the driver does not output a control signal, and the system outputs zero power. The equivalent output power of the system is $P_{\mathrm{eq}} = DP_{\mathrm{o}}$, where D is the ratio of the rated output power time to the period T. Hence, the equivalent output power can be adjusted by changing D.

The high misalignment tolerance of the self-oscillation WPT system with S/PS topology is determined by the essential characteristics of the S/PS topology WPT system. That is to say, when the S/PS topology WPT system satisfies the compensation equation $1/\sqrt{L_t C_t} = 1/\sqrt{L_r C_{\mathrm{req}}}$ and the input impedance is pure resistance, its output is independent of the coupling coefficient, which is the inherent characteristic of the S/PS topology WPT system. The purpose of adopting the self-oscillation control circuit in this article is to realize the second condition mentioned above, i.e., to ensure that the input impedance of the system is pure resistance.

A general conclusion can be drawn from the above analysis. Under the condition that the compensation equation is satisfied and the input impedance is pure resistance, if the output of a certain topology WPT system has nothing to do with the coupling coefficient, the system adopts the self-oscillation control circuit, which will have a high misalignment tolerance.

The self-oscillation WPT systems with other topologies are studied.

1) Four kinds of self-oscillation WPT systems with basic topologies are studied, and their schematic diagrams are shown in Fig. 9.

The output characteristics of four self-oscillation WPT systems with basic topologies can be derived from the coupled mode theory, and the comparison of the transmission characteristics of four self-oscillation WPT systems with basic topologies is listed in Table I.

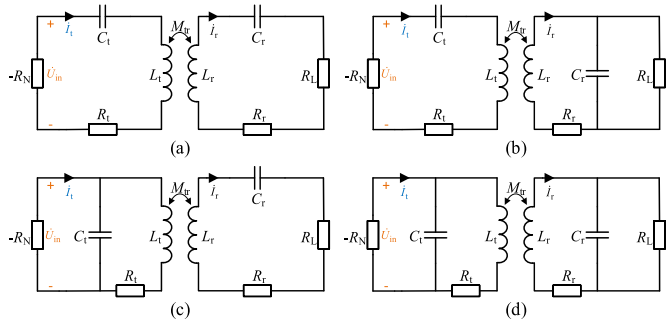

Fig. 9. Equivalent circuits of four self-oscillation WPT systems with basic topologies: (a) S/S. (b) S/P. (c) P/S. (d) P/P.

It can be seen from Table I that the output of four self-oscillation WPT systems with basic topologies is independent of the coupling coefficient, and they have high misalignment tolerance. It is verified that the output of the four basic topology WPT systems is independent of the coupling coefficient under the condition that the compensation equation is satisfied and the input impedance is pure resistance, so that when the four basic topology WPT systems adopt the self-oscillation control circuit, they have high misalignment tolerance.

1) For higher-order topology WPT systems. As long as the high-order topology can be equivalent to one of the four basic topologies, the high-order topology WPT system adopts the self-oscillation control circuit, which will have antimisalignment tolerance capability.

For example, S/PS topology. In this article, the S/PS topology is equivalent to the S/S topology by using the equivalent coupled-mode method. Since the output of the S/S topology WPT system is independent of the coupling coefficient under the condition that the compensation equation is satisfied and the input impedance is pure resistance, the self-oscillation WPT system with S/PS topology has high misalignment tolerance.

B. Design of System Parameters

When the coupling coefficient of the system satisfies $k > k_{\mathrm{c}}$, the output of the system is insensitive to the coupling coefficient. k_c determines the stable transmission range of the system, the smaller the k_c, the larger the stable transmission range of the system. From (18), it can be seen that the critical coupling coefficient is positively correlated with C_r, and negatively correlated with L_r and γ. It can be seen from (24) that the output voltage of the system is positively correlated with the receiving coil inductance L_r and the ratio γ of C_1 to C_r and is negatively correlated with the transmitting coil inductance L_t.

From the above analysis, the parameter design process of the proposed system can be obtained, and the specific design process is as follow.

1) Determine the maximum receiving coil inductance.

The height and diameter of the receiving coil can be acquired based on the space reserved for the receiving coil. The inductance formula of the space spiral coil is [43]

$$L = \frac{\pi \mu_0 K_N D_r^2 N^2}{4h} \tag{25}$$

where D_r is the diameter of the coil, and $\mu_0 = 4\pi \times 10^{-7}$ is the vacuum permeability. K_N is the coefficient of space spiral coil, and N is the number of turns of the coil. $h = (N-1)p_1 + D_1$ represents height of the coil, and D_1 is the diameter of the wire, and p_1 is the turn pitch.

Since the height of the coil is known, the maximum number of turns can be obtained when the turn pitch p_1 is equal to the diameter D_1 of the wire. Thus, the maximum receiving coil inductance can be calculated from (25).

2) Determine the minimum coupling coefficient $k_{\min}$ of the system.

The coupling coefficient with various transmission distance and misalignment can be calculated based on Neumann's formula [44]. Hence, the minimum coupling coefficient $k_{\min}$ of the system is determined according to the highest design requirements of transmission distance and misalignment.

3) Determine the compensation capacitors C_r and C_1.

According to (18), C_r and γ are adjusted to ensure that the critical coupling coefficient k_c is less than the minimum coupling coefficient $k_{\min}$. At this time, the output voltage and efficiency of the system are independent of the coupling coefficient.

Here, C_r can be set as a capacitance value that is easily available in the market, and then the critical coupling coefficient k_c can be adjusted to be smaller than the minimum coupling coefficient $k_{\min}$ by changing γ. When C_r and γ are determined, C_1 can be calculated based on $\gamma = C_1/C_r$.

4) Determine the transmitting coil inductance L_t and compensation capacitor C_t.

On the basis of (24), the output voltage U_o is adjusted to be equal to the design value U_{oset} of the output voltage by changing the transmitting coil inductance L_t.

Finally, C_t can be calculated according to the determined L_t, L_r, C_r, C_1 and compensation equation $1/\sqrt{L_t C_t} = 1/\sqrt{L_r(C_r + C_1)}$. So far, the system parameter design has been completed.

Furthermore, in order to clearly demonstrate the system parameter design process, the system parameter design flowchart is drawn, as shown in Fig. 10.

The above system parameter design process is applicable to the case where the load resistance is fixed. When the load resistance changes, only the third step of the above system parameter design process needs to be modified. It can be observed from (18) that the critical coupling coefficient of the system is positively correlated with the load resistance. When the load resistance increases, the critical coupling coefficient of the system increases. Assuming that the variation range of the load resistance is $R_{L\min} \le R_L \le R_{L\max}$, the corresponding variation range of the critical coupling coefficient is $k_{c\min} \le k_c \le k_{c\max}$. Where the critical coupling coefficient corresponding to $R_{L\min}$ is $k_{c\min}$, and the critical coupling coefficient corresponding to $R_{L\max}$ is $k_{c\max}$. The critical coupling coefficient can be adjusted by changing C_r and γ to ensure that the maximum critical coupling coefficient $k_{c\max}$ is less than the minimum coupling coefficient $k_{\min}$. At this time, when the load resistance changes within the range of $R_{L\min} \le R_L \le R_{L\max}$, the system always works in the strong coupling region, thus the output voltage has the antimisalignment ability.

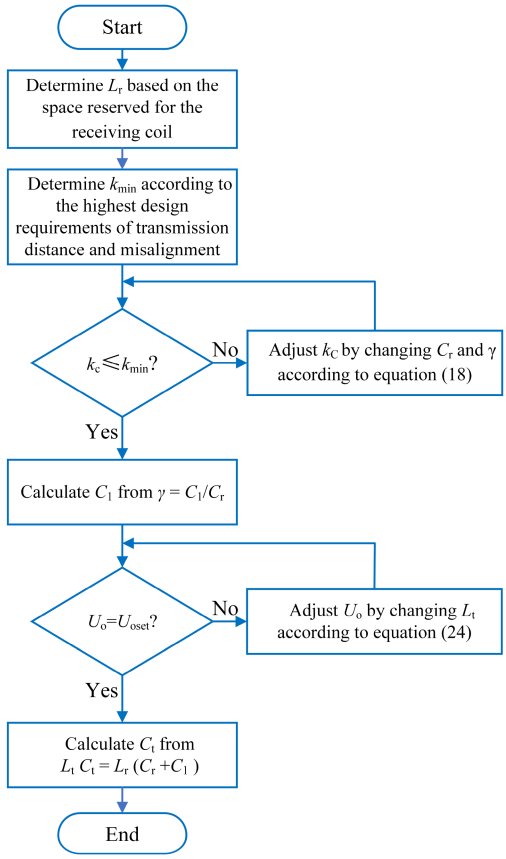

Fig. 10. System parameter design flowchart.

IV. Experimental Validation

To validate the theoretical analysis, an experimental prototype is constructed, as depicted in Fig. 11. The experimental parameters of the proposed WPT system are provided in Table II. The self-oscillation control method is adopted in this article, and the specific implementation process of the self-oscillation control method is as follows: The current transformer is used to sample the current of the transmitting circuit, and the turns ratio of the current transformer is 1:1:50. The differential sampling circuit is adopted to amplify the current signal, and the differential sampling circuit is composed of an operational amplifier model LMH6628. The amplified current signal is compared with the zero potential by the comparator to generate the drive signal, and the type of the comparator is TL3016. The drive signal controls the on and off of the MOSFET after passing through the driver, and the model of the driver is LM5109, and the type of MOSFET is VSP007N07MS. The control signal of S_1 is the same as the control signal of S_4, and the control signal of S_2 is identical to that of S_3. The phase difference between the control

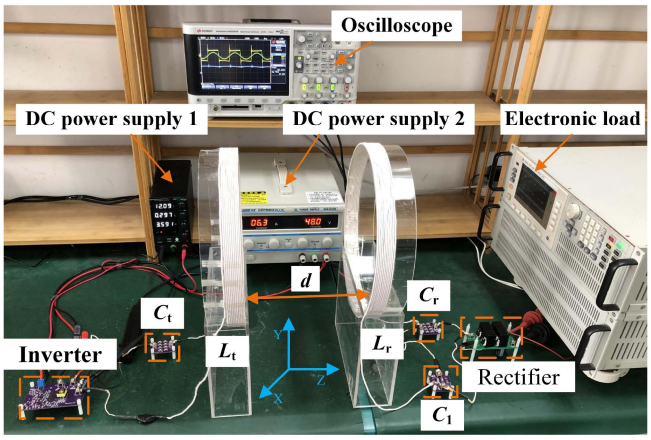

Fig. 11. Experimental prototype of the proposed WPT system.

signals of S_1 and S_4 and control signals of S_2 and S_3 is 180 degrees. The self-oscillation control method makes the output voltage and output current of the inverter have the same phase. At the same time, with the change in the coupling coefficient, the method can automatically adjust the working frequency to make the output basically constant. Furthermore, both the transmitting and receiving coils adopt spatial spiral coils in the prototype. It should be pointed out that the proposed system is applicable to all coils, including double-D coils and solenoids. The type of diode in the rectifier is SBR40U100CT.

The startup process of the self-oscillation inverter is as follows: After supplying power to the main circuit and the self-oscillation circuit, due to the slight disturbance of the signal at the negative input terminal of the comparator, even if the inverter has no current, the comparator will output an irregular rectangular wave, which controls the inverter start-up through the driver. At this time, the inverter has current. The current transformer and differential sampling circuit will detect the current in the inverter. After the detected current passes through the zero-crossing comparator, a control signal in phase with the inverter current will be generated, and the control signal will drive the inverter to work and keep oscillating.

According to the Hamel locus method, the system operates stably at both high frequency f_H and low frequency f_L. As the coupling coefficient changes, the proposed system will randomly select the high frequency branch f_H or the low frequency branch f_L to follow base on the equation $f = (\omega_t \pm \sqrt{\kappa^2 - \tau_r^2})/2\pi$. Hence, the system may jump between high frequency f_H and low frequency f_L with the change of coupling coefficient.

In practical applications, if the system is desired to work only at high frequency f_H or only at low frequency f_L, the system is prevented from jumping between high frequency and low frequency, and the self-oscillation control method can be improved to achieve this goal.

Compared with the self-oscillation control circuit in Fig. 1, the improved self-oscillation control circuit adds a microcontroller after the zero-crossing comparator. The working process of the improved self-oscillation control method will be described in detail below by taking the operation at high frequency as an example. The microcontroller detects the rising edge of the output signal of the zero-crossing comparator to track the phase of the inverter current. At the same time, the microcontroller detects the frequency of the output signal of the zero-crossing comparator and then judges whether the detected frequency f_d is greater than f_t. Where $f_t = \omega_t/2\pi$ is the natural resonance frequency. If the detected frequency f_d is greater than f_t, it is determined that the detected frequency f_d is high frequency f_H, and the microcontroller outputs the PWM signal with the detected frequency f_d. If the detected frequency f_d is less than f_t, it is determined that the detected frequency f_d is low frequency f_L, and the microcontroller outputs the PWM signal with a frequency of $(2f_t - f_d)$. Here, $(2f_t - f_d) = (2f_t - f_L) = f_H$. Thus, the system works only at the high frequency branch f_H.

The same method can be used to make the system work only at the low frequency branch f_L. The microcontroller detects the frequency of the output signal of the zero-crossing comparator and then judges whether the detected frequency f_d is less than f_t. If the detected frequency f_d is less than f_t, it is determined that the detected frequency f_d is low frequency f_L, and the microcontroller outputs the PWM signal with the detected frequency f_d. If the detected frequency f_d is greater than f_t, it is determined that the detected frequency f_d is high frequency f_H, and the microcontroller outputs the PWM signal with a frequency of $(2f_t - f_d)$. So then, the system works only at the low frequency branch f_L.

When $R_o = 12.3\ \Omega$ and the coils are aligned, the experimental waveforms of the output voltage versus distance are described in Fig. 12. It can be observed from Fig. 12 that the phase of the output voltage of the inverter is the same as that of the output current. Hence, the inverter is equivalent to the negative resistance.

The relationship curves between system performance and distance when $R_o = 12.3\ \Omega$, and the coils are aligned are depicted in Fig. 13. From Fig. 13(a), it can be seen that when the coils are aligned and the distance between the coils is less than 26.1 cm, the output voltage of the system remains basically unchanged as the distance changes. Specifically, when the distance increases from 8.0 to 26.1 cm, the output voltage fluctuates by 0.97 V, which is 1.6% of the rated output voltage. The experimental value of the critical transmission distance is 26.1 cm, and the corresponding experimental value of the critical coupling coefficient is 0.0478 (the relationship between the coupling coefficient and the transmission distance is surveyed by the impedance analyzer). According to (18), the theoretical value of the critical coupling coefficient is 0.0444, and the corresponding theoretical value of the critical transmission distance is 26.9 cm. The experimental results are basically consistent with the theoretical results.

The equation $P_o = U_o^2/R_o$ is used to calculate the experimental value of the output power. The dc output voltage U_o is directly read from the oscilloscope (InfiniiVision DSOX2014A), so that the experimental value of the output power can be obtained. The theoretical value of output power is calculated according to (20).

The solid line in Fig. 13(b) indicates the theoretical result, and the black rhombus in Fig. 13(b) represents the experimental

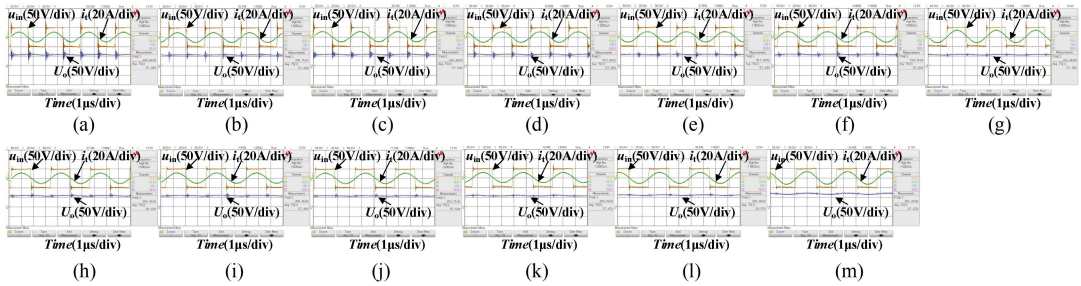

Fig. 12. Experimental waveforms of the output voltage versus distance when $R_o = 12.3\ \Omega$ and the coils are aligned. (a) $d = 8$ cm. (b) $d = 10$ cm. (c) $d = 12$ cm. (d) $d = 14$ cm. (e) $d = 16$ cm. (f) $d = 18$ cm. (g) $d = 20$ cm. (h) $d = 22$ cm. (i) $d = 24$ cm. (j) $d = 26$ cm. (k) $d = 26.1$ cm. (l) $d = 28$ cm. (m) $d = 30$ cm.

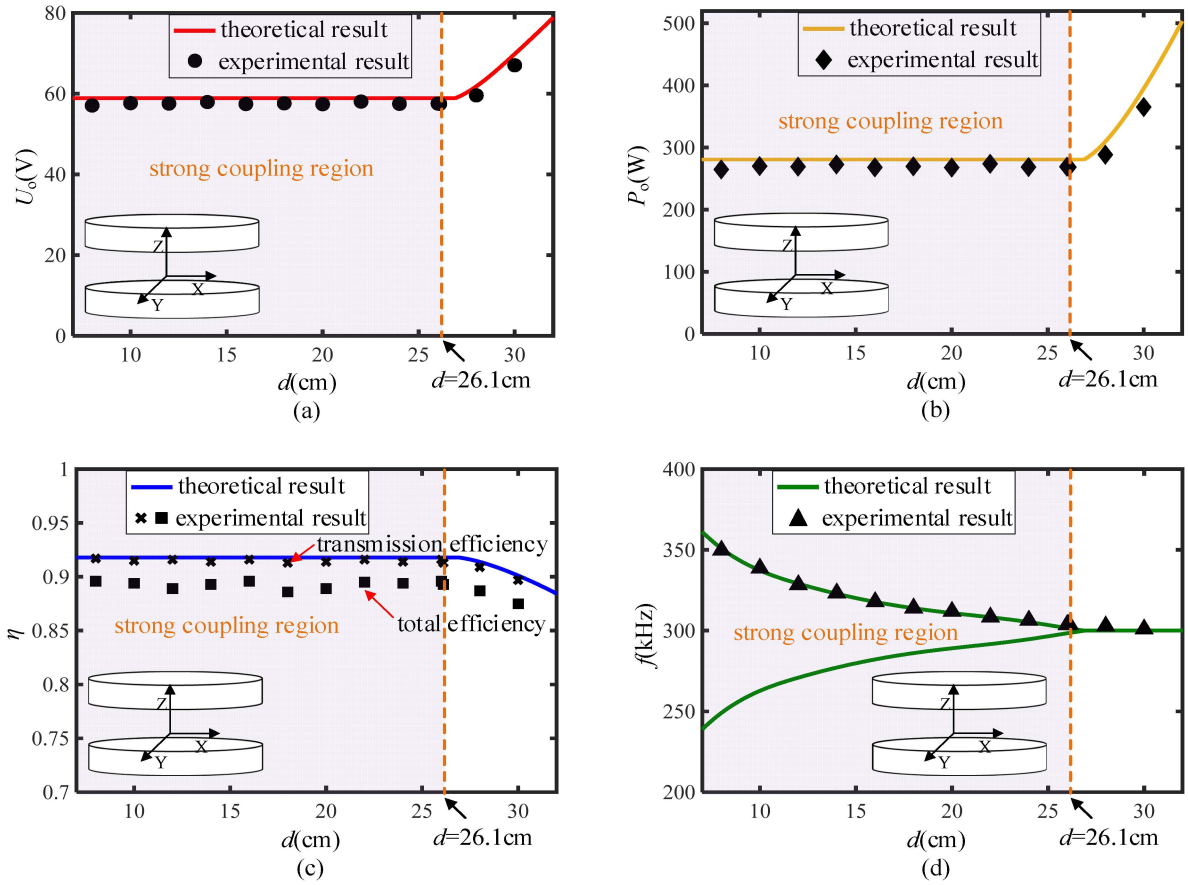

Fig. 13. Relationship curves between system performance and distance when $R_o = 12.3\ \Omega$ and the coils are aligned. (a) Output voltage. (b) Output power. (c) Efficiency. (d) Working frequency.

result. It can be seen from Fig. 13(b) that the experimental results of the output power are basically consistent with the theoretical results. In the strong coupling region, the average value of the experimental results of the output power is 269.3 W. When the coils are aligned and the distance between the coils is less than 26.1 cm, the output power of the system is almost unchanged with the change in the distance. Specifically, when the distance increases from 8.0 to 26.1 cm, the output power fluctuates by 9.1 W, which is 3.2% of the rated output power. Therefore, the proposed WPT system has a high misalignment tolerance in the Z-direction.

In this work, the equation $\eta_{\text{total-exp}} = U_o^2/(V_{DC} I_{DC} R_o)$ is used to calculate the experimental value of the total efficiency. The values of the dc input voltage V_{DC} and dc input current I_{DC} are directly read from the dc power supply 2 (KXN-6030D), so then the experimental value of the total efficiency can be calculated. The experimental value of transmission efficiency is calculated by the equation $\eta_{\text{tra-exp}} = \pi^3 U_L^2/(16\sqrt{2} V_{DC} I_t R_o)$ [42]. The RMS values of the equivalent ac output voltage U_L and inverter output current I_t are directly read from the oscilloscope. The theoretical value of the transmission efficiency is calculated from (21).

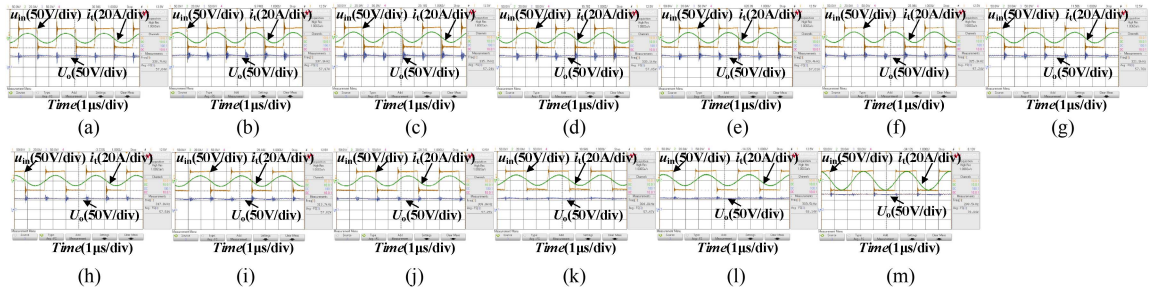

Fig. 14. Experimental waveforms of the output voltage versus misalignment when $R_o = 12.3\ \Omega$ and $d = 10$ cm. (a) Misalignment is 0 cm. (b) Misalignment is 2 cm. (c) Misalignment is 4 cm. (d) Misalignment is 6 cm. (e) Misalignment is 8 cm. (f) Misalignment is 10 cm. (g) Misalignment is 12 cm. (h) Misalignment is 14 cm. (i) Misalignment is 16 cm. (j) Misalignment is 18 cm. (k) Misalignment is 19.8 cm. (l) Misalignment is 20 cm. (m) Misalignment is 22 cm.

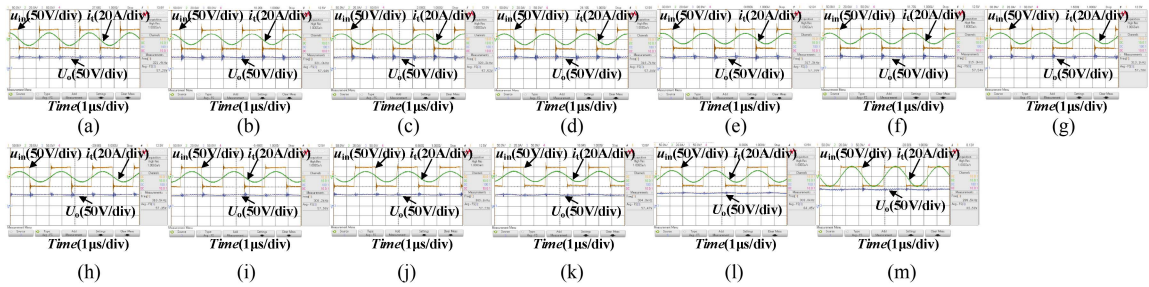

Fig. 15. Experimental waveforms of the output voltage versus misalignment when $R_o = 12.3\ \Omega$ and $d = 15$ cm. (a) Misalignment is 0 cm. (b) Misalignment is 2 cm. (c) Misalignment is 4 cm. (d) Misalignment is 6 cm. (e) Misalignment is 8 cm. (f) Misalignment is 10 cm. (g) Misalignment is 12 cm. (h) Misalignment is 14 cm. (i) Misalignment is 16 cm. (j) Misalignment is 18 cm. (k) Misalignment is 18.2 cm. (l) Misalignment is 20 cm. (m) Misalignment is 22 cm.

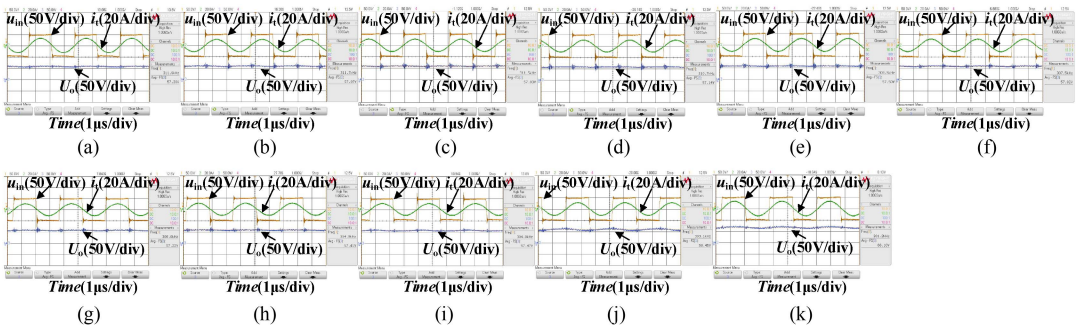

Fig. 16. Experimental waveforms of the output voltage versus misalignment when $R_o = 12.3\ \Omega$ and $d = 20$ cm. (a) Misalignment is 0 cm. (b) Misalignment is 2 cm. (c) Misalignment is 4 cm. (d) Misalignment is 6 cm. (e) Misalignment is 8 cm. (f) Misalignment is 10 cm. (g) Misalignment is 12 cm. (h) Misalignment is 14 cm. (i) Misalignment is 14.9 cm. (j) Misalignment is 16 cm. (k) Misalignment is 18 cm.

The solid line in Fig. 13(c) represents the theoretical result of transmission efficiency, the black cross in Fig. 13(c) indicates the experimental result of transmission efficiency, and the black square in Fig. 13(c) represents the experimental result of total efficiency. From Fig. 13(c), it can be seen that the experimental result of the transmission efficiency is basically consistent with the theoretical result, so that the accuracy of the efficiency calculation of the experimental results is verified.

Furthermore, as can be seen from Fig. 13(d), the system will automatically track the working frequency $f = (\omega_t \pm \sqrt{\kappa^2 - \tau_r^2})/2\pi$ with the change of the distance.

When $R_o = 12.3\ \Omega$ and $d = 10$ cm, the experimental waveforms of the output voltage versus misalignment are described in Fig. 14. Fig. 15 presents the experimental waveforms of the output voltage versus misalignment when $R_o = 12.3\ \Omega$ and $d = 15$ cm. When $R_o = 12.3\ \Omega$ and $d = 20$ cm, the experimental waveforms of the output voltage versus misalignment are shown in Fig. 16.

The curves of system performance versus misalignment at different distances when $R_o = 12.3\ \Omega$ are illustrated in Fig. 17. It can be observed from Fig. 17 that when the distance is 20.0 cm and the misalignment is less than 14.9 cm, the output voltage fluctuates by 0.83 V, the output power fluctuates by 7.8 W, and the efficiency fluctuates by 1.1%. That is, the output voltage, output power and efficiency of the system are basically constant. Consequently, the proposed WPT system has a high misalignment tolerance in the X-direction and Y-direction.

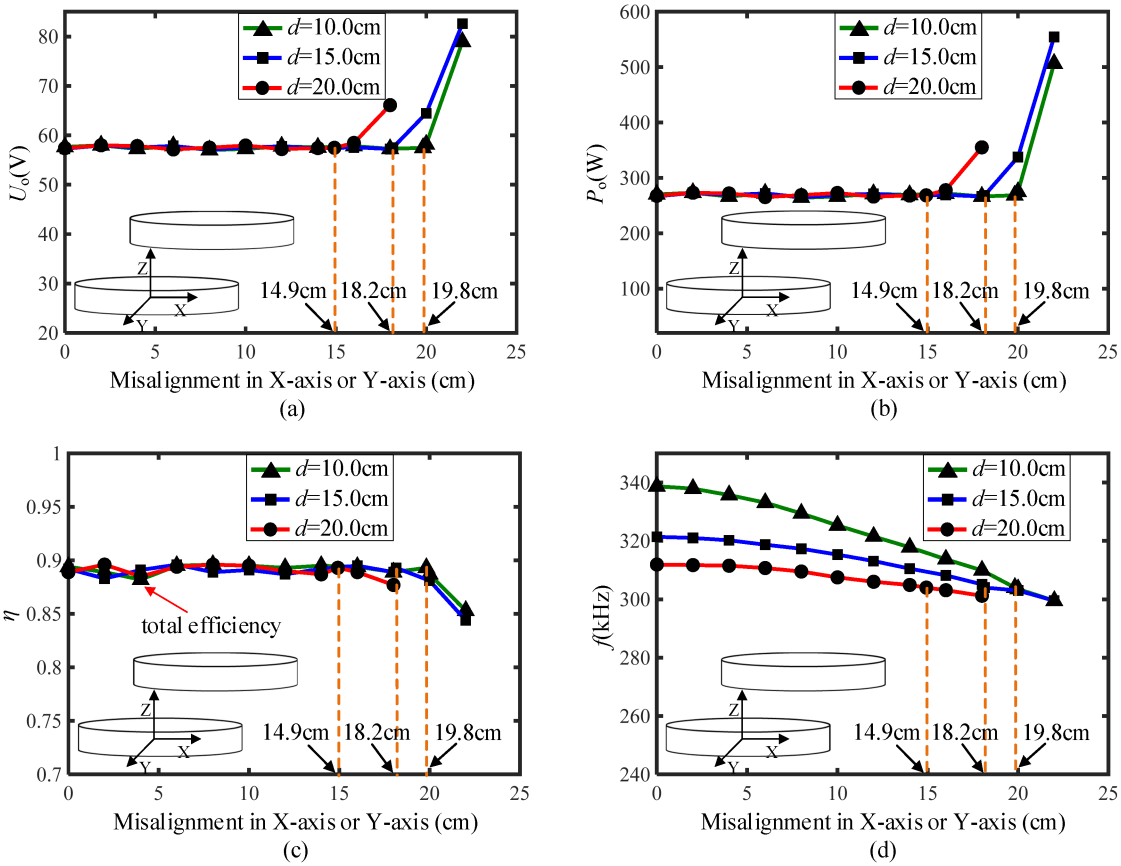

Fig. 17. Curves of system performance versus misalignment at different distances when R_o = 12.3 Ω. (a) Output voltage. (b) Output power. (c) Efficiency. (d) Working frequency.

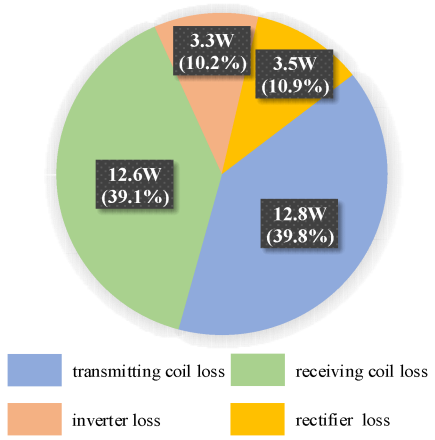

Fig. 18. Loss analysis of the system.

The loss analysis of the system is described in Fig. 18. The power loss of the system mainly includes transmitting coil loss, inverter loss, receiving coil loss, and rectifier loss. The system efficiency is 89.3%, and the total loss is 32.2 W.

Besides, experiments with different load resistances are provided. The dc load resistances are set to 12.3, 20, and 30 Ω, respectively. Other experimental parameters are the same as those in Table II.

Fig. 19 presents the experimental waveforms of the output voltage versus distance when R_o = 20 Ω and the coils are aligned. When R_o = 30 Ω and the coils are aligned, the experimental waveforms of the output voltage versus distance are illustrated in Fig. 20. When R_o = 20 Ω and d = 10 cm, the experimental waveforms of the output voltage versus misalignment are depicted in Fig. 21. Fig. 22 is the experimental waveforms of the output voltage versus misalignment when R_o = 30 Ω and d = 10 cm. The experimental results of output voltage versus distance and misalignment under different load resistances are shown in Fig. 23.

It can be observed from Figs. 12, 19, 20, and 23(a) that when R_o = 12.3 Ω, the critical transmission distance is 26.1 cm. When R_o = 20 Ω, the critical transmission distance is 20.8 cm. When R_o = 30 Ω, the critical transmission distance is 16.6 cm. When the transmission distance d is less than the critical transmission distance, the system operates in the strong coupling region. For different load resistances, the output voltage in the strong coupling region remains basically unchanged as the distance changes. In addition, when the transmission distance is less than 16.6 cm and the dc load resistance changes from 12.3 to 30 Ω, the output voltage fluctuates by 3.4 V, and the voltage fluctuation is small. Therefore, in the strong coupling region, the output voltage of the system is insensitive to the load resistance and transmission distance.

It can be seen from Figs. 14, 21, 22, and 23(b) that when R_o = 12.3 Ω, d = 10 cm, and the misalignment is less than 19.8 cm, the

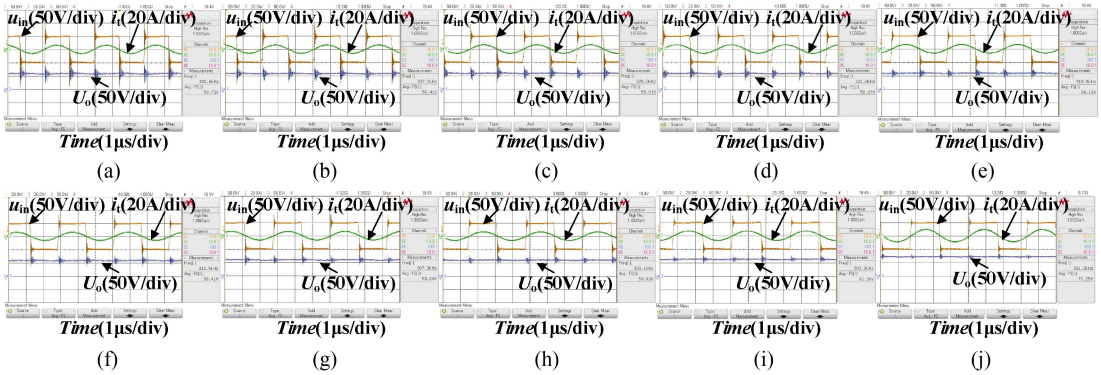

Fig. 19. Experimental waveforms of the output voltage versus distance when $R_o = 20\ \Omega$ and the coils are aligned. (a) $d = 8$ cm. (b) $d = 10$ cm. (c) $d = 12$ cm. (d) $d = 14$ cm. (e) $d = 16$ cm. (f) $d = 18$ cm. (g) $d = 20$ cm. (h) $d = 20.8$ cm. (i) $d = 22$ cm. (j) $d = 24$ cm.

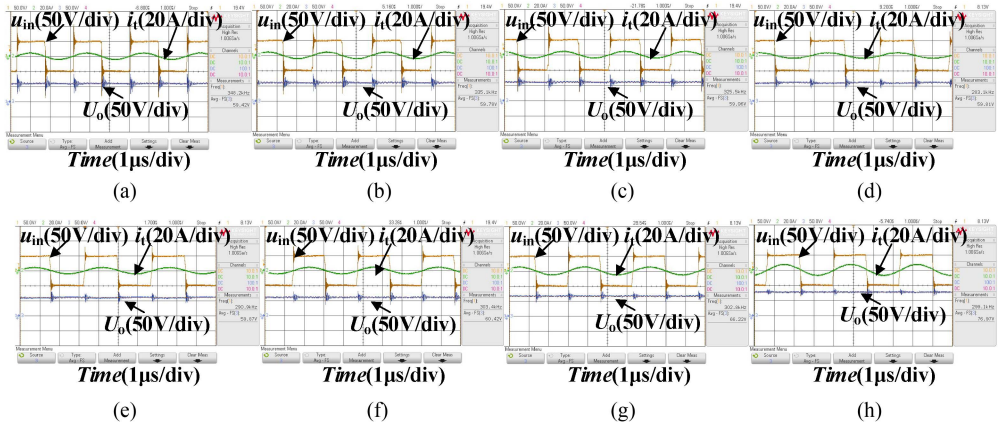

Fig. 20. Experimental waveforms of the output voltage versus distance when $R_o = 30\ \Omega$ and the coils are aligned. (a) $d = 8$ cm. (b) $d = 10$ cm. (c) $d = 12$ cm. (d) $d = 14$ cm. (e) $d = 16$ cm. (f) $d = 16.6$ cm. (g) $d = 18$ cm. (h) $d = 20$ cm.

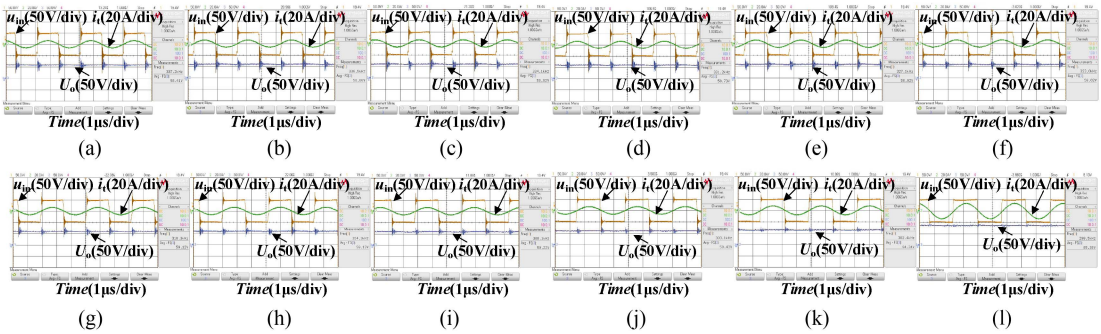

Fig. 21. Experimental waveforms of the output voltage versus misalignment when $R_o = 20\ \Omega$ and $d = 10$ cm. (a) Misalignment is 0 cm. (b) Misalignment is 2 cm. (c) Misalignment is 4 cm. (d) Misalignment is 6 cm. (e) Misalignment is 8 cm. (f) Misalignment is 10 cm. (g) Misalignment is 12 cm. (h) Misalignment is 14 cm. (i) Misalignment is 16 cm. (j) Misalignment is 16.9 cm. (k) Misalignment is 18 cm; (l) Misalignment is 20 cm.

system operates in the strong coupling region. When $R_o = 20\ \Omega$, $d = 10$ cm, and the misalignment is less than 16.9 cm, the system works in the strong coupling region. When $R_o = 30\ \Omega$, $d = 10$ cm, and the misalignment is less than 13.6 cm, the system works in the strong coupling region. For different load resistances, the output voltage in the strong coupling region remains essentially unchanged with the variation of misalignment. In summary, when the load resistance changes, as long as the proposed WPT system operates in the strong coupling region, the system has antimisalignment tolerance capability.

The main differences between this work and literature [36] are as follows.

1) The principle is different. The system in [36] is the PT-symmetric WPT system, while the system proposed in this

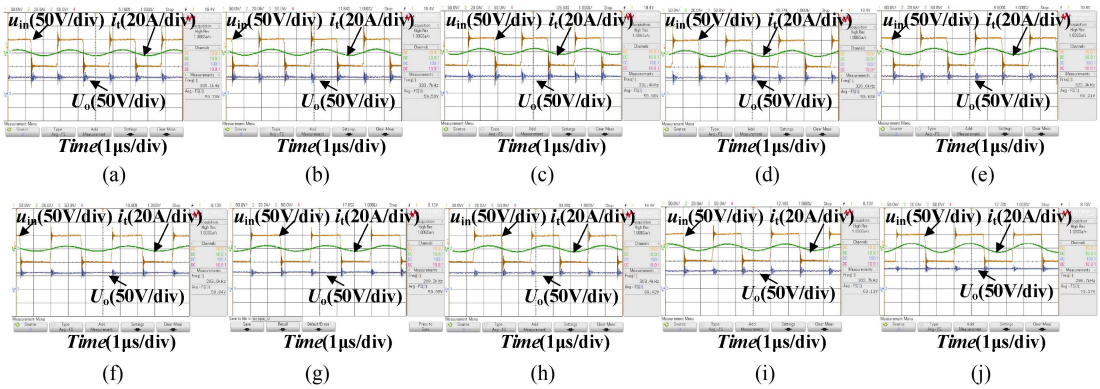

Fig. 22. Experimental waveforms of the output voltage versus misalignment when $R_o = 30\ \Omega$ and $d = 10$ cm. (a) Misalignment is 0 cm. (b) Misalignment is 2 cm. (c) Misalignment is 4 cm. (d) Misalignment is 6 cm. (e) Misalignment is 8 cm. (f) Misalignment is 10 cm. (g) Misalignment is 12 cm. (h) Misalignment is 13.6 cm. (i) Misalignment is 14 cm. (j) Misalignment is 16 cm.

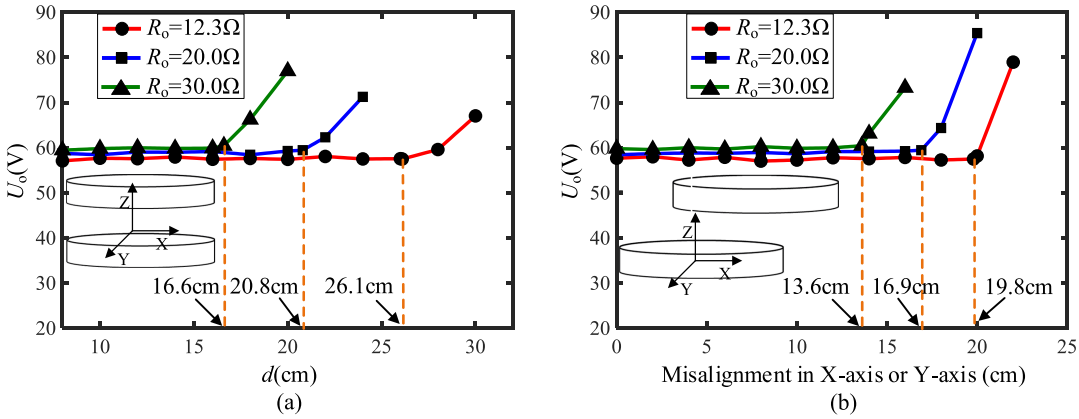

Fig. 23. Experimental results of output voltage versus distance and misalignment under different load resistances. (a) Experimental results of output voltage versus distance under different load resistances when the coils are aligned. (b) Experimental results of output voltage versus misalignment under different load resistances when $d = 10$ cm.

article is not a PT-symmetric WPT system. The output voltage and efficiency of the self-oscillation WPT system with S/PS topology in the strong coupling region are not sensitive to the coupling coefficient. Although this characteristic is similar to that of the PT-symmetric WPT system, the proposed system changes under the joint parity and time reversal operations, and according to the definition of PT-symmetry, the proposed system is not PT-symmetry. The system in [36] remains unchanged under the joint parity and time reversal operations, and the system in [36] is PT-symmetry.

2) The modeling method is different. Zhou et al. [36] adopts the traditional coupled-mode method to model and analyze the WPT system with S/S compensation topology, while this article adopts the proposed equivalent coupled-mode method to model and analyze the WPT system with S/PS compensation topology. The traditional coupled-mode method can only model and analyze the WPT system with first-order compensation topology, but it cannot model and analyze the WPT system with S/PS compensation topology. Besides, the expressions for the output voltage and efficiency of the S/PS compensation topology WPT system derived from circuit theory are very complicated, and the expression for the critical coupling coefficient cannot be derived from circuit theory. In order to simplify the expressions for the output voltage and efficiency of the proposed system and derive the expression for the critical coupling coefficient, this article proposes an equivalent coupled-mode method.

3) Compared with literature [36], the stable transmission range of the system proposed in this article is wider. The coupling coefficient in literature [36] needs to satisfy $k > \frac{R_r+R_L}{\omega_t L_r}$, and the coupling coefficient in this article needs to satisfy $k > \frac{R_r+\frac{C_r^2}{(C_r+C_1)^2}R_L}{\omega_t L_r}$. Consequently, the stable transmission range of this artcle is larger than that of literature [36].

In order to clearly compare the methods for improving misalignment tolerance, a comparison table is given, as shown in Table III.

From Table III, it can be seen that compared with existing methods, the proposed method has the following advantages.

1) The proposed method can realize ZPA, has unity power factor, and improves power transmission capability.

TABLE III
COMPARISON OF DIFFERENT METHODS

Method	Reference	Compensation network	Coil size and distance (mm)	ZPA	Misalignment tolerant range	Misalignment tolerant in all directions	Fluctuation range of efficiency and output
Optimizing the structure of the magnetic coupler	[25]	S/S	Transmitting:612.4×250 Receiving:512.4×250 Distance: 120	No	x-misalignment:0 to 400mm y-misalignment: 0 to 100mm z-misalignment: 0 to 50mm	No	Efficiency:5.4% Output current:1.4%
	[26]	LCC/S	Transmitting:250×209 Receiving: 250×209 Distance: 50	No	x-misalignment: 0 to 140mm y-misalignment: 0 to 110mm z-misalignment:N/A	No	Efficiency:1.1% Output voltage:6.6%
	[27]	S/LCC	Transmitting:450×450 Receiving: 450×450 Distance: 150	No	x-misalignment:0 to 250mm y-misalignment: N/A z-misalignment:-20 to 80mm	No	Efficiency:6.0% Output voltage:8.2%
Optimizing system parameters	[29]	S/SP	Transmitting: 208(diameter) Receiving: 206(diameter) Distance: 41	No	$0.211<k<0.355$	**Yes**	Efficiency:4.5% Output voltage:5.6%
	[30]	S/SP	Transmitting: N/A Receiving: N/A Distance: N/A	No	$0.140<k<0.285$	**Yes**	Efficiency:5.2% Output voltage:9.0%
	[31]	S/S/S/S	Transmitting:400×400 Receiving: 400×400 Distance: 200	No	x-misalignment:0 to 177mm y-misalignment: N/A z-misalignment: N/A	No	Efficiency:6.2% Output power:22%
Novel topological structures	[34]	LCLCL/LCLCL	Transmitting:775×391 Receiving: 775×391 Distance: 120	No	x-misalignment:-80 to 120mm y-misalignment: -160 to 160 z-misalignment: -20 to 20	**Yes**	Efficiency:6.8% Output power:5.0%
	[35]	LCC/S	Transmitting: N/A Receiving: N/A Distance: 80	No	x-misalignment:0 to 90mm y-misalignment: N/A z-misalignment: N/A	No	Efficiency:0.8% Output power:8.1%
PT-symmetry principle	[36]	S/S	Transmitting:260(diameter) Receiving:140(diameter) Distance: <100	**Yes**	$k > \frac{R_r + R_L}{\omega_t L_r}$ (k>0.1)	**Yes**	Efficiency: 0.9% Output power:1.0%
Self-oscillation control method	This work	S/PS	Transmitting:300(diameter) Receiving:300(diameter) Distance: <261	**Yes**	$k > \frac{R_r + \frac{C_r^2}{(C_r + C_1)^2} R_L}{\omega_t L_r}$ (k>0.0478)	**Yes**	Efficiency:1.3% Output voltage: 1.6%

* N/A indicates not available

2) The proposed method has high misalignment tolerance in all directions, which increases spatial freedom.
3) The output voltage and efficiency fluctuations of the proposed method in the strong coupling region are small, and the efficiency fluctuation is 1.3%, and the output voltage fluctuation is 1.6%.
4) Compared with the PT-symmetric WPT system, the stable transmission region of the proposed system is wider.

V. CONCLUSION

A high misalignment tolerance WPT system is proposed in this work. The output voltage and efficiency of the S/PS topology WPT system in the strong coupling region are not sensitive to the coupling coefficient under the condition that the compensation equation is satisfied and the input impedance is pure resistance. The proposed system adopts the self-oscillation control method to achieve negative resistance, and the system has a unity power factor and high system efficiency. Moreover, an equivalent coupled-mode method is presented, which can effectively model and analyze WPT systems with high-order compensation topology. Finally, a laboratory prototype to constructed. When the coils are aligned and the distance increases from 8.0 to 26.1 cm, the output voltage fluctuates by 0.97 V, the output power fluctuates by 9.1 W, and the efficiency fluctuates by 1.3%. When the distance is 20.0 cm and the misalignment is less than 14.9 cm, the output voltage, output power, and efficiency of the system remain essentially unchanged. Consequently, the proposed WPT system has a high misalignment tolerance in the X-direction, Y-direction, and Z-direction.

REFERENCES

[1] Z. Yan, B. Song, Y. Zhang, K. Zhang, Z. Mao, and Y. Hu, "A rotation-free wireless power transfer system with stable output power and efficiency for autonomous underwater vehicles," *IEEE Trans. Power Electron.*, vol. 34, no. 5, pp. 4005–4008, May 2019.

[2] J. Zhou, P. Yao, Y. Chen, K. Guo, S. Hu, and H. Sun, "Design considerations for a self-latching coupling structure of inductive power transfer for autonomous underwater vehicle," *IEEE Trans. Ind. Appl.*, vol. 57, no. 1, pp. 580–587, Jan./Feb. 2021.

[3] Y. Zeng et al., "Misalignment insensitive wireless power transfer system using a hybrid transmitter for autonomous underwater vehicles," *IEEE Trans. Ind. Appl.*, vol. 58, no. 1, pp. 1298–1306, Jan./Feb. 2022.

[4] J. Kim, K. Kim, H. Kim, D. Kim, J. Park, and S. Ahn, "An efficient modeling for underwater wireless power transfer using Z-parameters," *IEEE Trans. Electromagn. Compat.*, vol. 61, no. 6, pp. 2006–2014, Dec. 2019.

[5] Y.-C. Hsieh, Z.-R. Lin, M.-C. Chen, H.-C. Hsieh, Y.-C. Liu, and H.-J. Chiu, "High-efficiency wireless power transfer system for electric vehicle applications," *IEEE Trans. Circuits Syst. II-Exp. Briefs*, vol. 64, no. 8, pp. 942–946, Aug. 2017.

[6] H. Li, Y. Yang, J. Chen, J. Xu, M. Liu, and Y. Wang, "A hybrid class-E topology with constant current and constant voltage output for light EVs wireless charging application," *IEEE Trans. Transp. Electrif.*, vol. 7, no. 4, pp. 2168–2180, Dec. 2021.

[7] A. Ahmad, M. S. Alam, and R. Chabaan, "A comprehensive review of wireless charging technologies for electric vehicles," *IEEE Trans. Transp. Electrif.*, vol. 4, no. 1, pp. 38–63, Mar. 2018.

[8] Y. Zhang et al., "Misalignment-tolerant dual-transmitter electric vehicle wireless charging system with reconfigurable topologies," *IEEE Trans. Power Electron.*, vol. 37, no. 8, pp. 8816–8819, Aug. 2022.

[9] B. Regensburger, S. Sinha, A. Kumar, S. Maji, and K. K. Afridi, "High-performance multi-MHz capacitive wireless power transfer system for EV charging utilizing interleaved-foil coupled inductors," *IEEE J. Emerg. Sel. Topics Power Electron.*, vol. 10, no. 1, pp. 35–51, Feb. 2022.

[10] X. Li, Y. Li, C. Tsui, and W. Ki, "Wireless power transfer system with $\sigma\delta$- modulated transmission power and fast load response for implantable medical devices," *IEEE Trans. Circuits Syst. II-Exp. Briefs*, vol. 64, no. 3, pp. 279–283, Mar. 2017.
[11] C. Rong, B. Zhang, Z. Wei, L. Wu, and X. Shu, "A wireless power transfer system for spinal cord stimulation based on generalized parity–Time symmetry condition," *IEEE Trans. Ind. Appl.*, vol. 58, no. 1, pp. 1330–1339, Jan./Feb. 2022.
[12] S. Pal and W.-H. Ki, "40.68 MHz digital on-off delay-compensated active rectifier for WPT of biomedical applications," *IEEE Trans. Circuits Syst. II-Exp. Briefs*, vol. 67, no. 12, pp. 3307–3311, Dec. 2020.
[13] S. C. Tang, T. L. T. Lun, Z. Guo, K.-W. Kwok, and N. J. McDannold, "Intermediate range wireless power transfer with segmented coil transmitters for implantable heart pumps," *IEEE Trans. Power Electron.*, vol. 32, no. 5, pp. 3844–3857, May 2017.
[14] B. Yang et al., "Analysis and design of a T/S compensated IPT system for AGV maintaining stable output current versus air gap and load variations," *IEEE Trans. Power Electron.*, vol. 37, no. 5, pp. 6217–6228, May 2022.
[15] C. Zhu et al., "Analysis and design of cost-effective WPT systems with dual independently regulatable outputs for automatic guided vehicles," *IEEE Trans. Power Electron.*, vol. 36, no. 6, pp. 6183–6187, Jun. 2021.
[16] S. Pan, Y. Xu, Y. Lu, W. Liu, Y. Li, and R. Mai, "Design of compact magnetic coupler with low leakage EMF for AGV wireless power transfer system," *IEEE Trans. Ind. Appl.*, vol. 58, no. 1, pp. 1044–1052, Jan./Feb. 2022.
[17] E. S. Lee and S. H. Han, "2-D thin coil designs of IPT for wireless charging of automated guided vehicles," *IEEE J. Emerg. Sel. Topics Power Electron.*, vol. 10, no. 2, pp. 2629–2644, Apr. 2022.
[18] C. Jiang, K. T. Chau, C. Liu, C. H. T. Lee, W. Han, and W. Liu, "Move-and-charge system for automatic guided vehicles," *IEEE Trans. Magn.*, vol. 54, no. 11, pp. 1–5, Nov. 2018.
[19] C. Rong, B. Zhang, Y. Jiang, X. Shu, and Z. Wei, "A misalignment-tolerant fractional-order wireless charging system with constant current or voltage output," *IEEE Trans. Power Electron.*, vol. 37, no. 9, pp. 11356–11368, Sep. 2022.
[20] R. Mai, Y. Chen, Y. Li, Y. Zhang, G. Cao, and Z. He, "Inductive power transfer for massive electric bicycles charging based on hybrid topology switching with a single inverter," *IEEE Trans. Power Electron.*, vol. 32, no. 8, pp. 5897–5906, Aug. 2017.
[21] R. Mai, Y. Chen, Y. Zhang, N. Yang, G. Cao, and Z. He, "Optimization of the passive components for an S-LCC topology-based WPT system for charging massive electric bicycles," *IEEE Trans. Ind. Electron.*, vol. 65, no. 7, pp. 5497–5508, Jul. 2018.
[22] P. K. Joseph, D. Elangovan, and P. Sanjeevikumar, "System architecture, design, and optimization of a flexible wireless charger for renewable energy-powered electric bicycles," *IEEE Syst. J.*, vol. 15, no. 2, pp. 2696–2707, Jun. 2021.
[23] P. Tan, T. Peng, X. Gao, and B. Zhang, "Flexible combination and switching control for robust wireless power transfer system with hexagonal array coil," *IEEE Trans. Power Electron.*, vol. 36, no. 4, pp. 3868–3882, Apr. 2021.
[24] Y. Li, J. Zhao, Q. Yang, L. Liu, J. Ma, and X. Zhang, "A novel coil with high misalignment tolerance for wireless power transfer," *IEEE Trans. Magn.*, vol. 55, no. 6, pp. 1–4, Jun. 2019.
[25] Y. Yao, S. Gao, J. Mai, X. Liu, X. Zhang, and D. Xu, "A novel misalignment tolerant magnetic coupler for electric vehicle wireless charging," *IEEE J. Emerg. Sel. Topics Ind. Electron.*, vol. 3, no. 2, pp. 219–229, Apr. 2022.
[26] J. Mai, Y. Wang, Y. Yao, M. Sun, and D. Xu, "High-misalignment-tolerant IPT systems with solenoid and double D pads," *IEEE Trans. Ind. Electron.*, vol. 69, no. 4, pp. 3527–3535, Apr. 2022.
[27] W. Zhao, X. Qu, J. Lian, and C. K. Tse, "A family of hybrid IPT couplers with high tolerance to pad misalignment," *IEEE Trans. Power Electron.*, vol. 37, no. 3, pp. 3617–3625, Mar. 2022.
[28] J. Mai, Y. Wang, Y. Yao, and D. Xu, "Analysis and design of high-misalignment-tolerant compensation topologies with constant-current or constant-voltage output for IPT systems," *IEEE Trans. Power Electron.*, vol. 36, no. 3, pp. 2685–2695, Mar. 2021.
[29] Y. Wang, J. Mai, Y. Yao, and D. Xu, "Analysis and design of an IPT system based on S/SP compensation with improved output voltage regulation," *IEEE Trans. Ind. Inform.*, vol. 16, no. 5, pp. 3256–3266, May 2020.
[30] Q. Zhu, Y. Guo, L. Wang, C. Liao, and F. Li, "Improving the misalignment tolerance of wireless charging system by optimizing the compensate capacitor," *IEEE Trans. Ind. Electron.*, vol. 62, no. 8, pp. 4832–4836, Aug. 2015.
[31] Z. Yan et al., "Fault-tolerant wireless power transfer system with a dual-coupled LCC-S topology," *IEEE Trans. Veh. Technol.*, vol. 68, no. 12, pp. 11838–11846, Dec. 2019.
[32] L. Zhao, D. J. Thrimawithana, and U. K. Madawala, "Hybrid bidirectional wireless EV charging system tolerant to pad misalignment," *IEEE Trans. Ind. Electron.*, vol. 64, no. 9, pp. 7079–7086, Sep. 2017.
[33] L. Zhao, D. J. Thrimawithana, U. K. Madawala, A. P. Hu, and C. C. Mi, "A misalignment-tolerant series-hybrid wireless EV charging system with integrated magnetics," *IEEE Trans. Power Electron.*, vol. 34, no. 2, pp. 1276–1285, Feb. 2019.
[34] R. Mai, B. Yang, Y. Chen, N. Yang, Z. He, and S. Gao, "A misalignment tolerant IPT system with intermediate coils for constant-current output," *IEEE Trans. Power Electron.*, vol. 34, no. 8, pp. 7151–7155, Aug. 2019.
[35] X. Qu, Y. Yao, D. Wang, S.-C. Wong, and C. K. Tse, "A family of hybrid IPT topologies with near load-independent output and high tolerance to pad misalignment," *IEEE Trans. Power Electron.*, vol. 35, no. 7, pp. 6867–6877, Jul. 2020.
[36] J. Zhou, B. Zhang, W. Xiao, D. Qiu, and Y. Chen, "Nonlinear parity-time-symmetric model for constant efficiency wireless power transfer: Application to a drone-in-flight wireless charging platform," *IEEE Trans. Ind. Electron.*, vol. 66, no. 5, pp. 4097–4107, May 2019.
[37] D. Wu, R. Mai, S. Zhao, Z. He, and F. Peng, "A self-oscillating controller based on pulse density modulator in wireless power transfer," in *Proc. IEEE Energy Convers. Congr. Expo.*, 2019, pp. 2125–2128.
[38] K. Yan, Q. Chen, J. Hou, X. Ren, and X. Ruan, "Self-oscillating contactless resonant converter with phase detection contactless current transformer," *IEEE Trans. Power Electron.*, vol. 29, no. 8, pp. 4438–4449, Aug. 2014.
[39] J. Ren, P. Hu, D. Yang, and D. Liu, "Tuning of mid-range wireless power transfer system based on delay-iteration method," *IET Power Electron*, vol. 9, no. 8, pp. 1563–1570, Jun. 2016.
[40] H. Li, K. Wang, L. Huang, W. Chen, and X. Yang, "Dynamic modeling based on coupled modes for wireless power transfer systems," *IEEE Trans. Power Electron.*, vol. 30, no. 11, pp. 6245–6253, Nov. 2015.
[41] S. Assawaworrarit, X. Yu, and S. Fan, "Robust wireless power transfer using a nonlinear parity–time-symmetric circuit," *Nature*, vol. 546, no. 7658, pp. 387–390, Jun. 2017.
[42] K. Song, Z. Li, J. Jiang, and C. Zhu, "Constant current/voltage charging operation for series–Series and series–Parallel compensated wireless power transfer systems employing primary-side controller," *IEEE Trans. Power Electron.*, vol. 33, no. 9, pp. 8065–8080, Sep. 2018.
[43] T. Chen, B. Liu, Y. Luo, and Y. Zhang, *Inductance Calculation Manual*. Beijing, China: Machinery Industry Press, 1992.
[44] F. Liu, Y. Yang, D. Jiang, X. Ruan, and X. Chen, "Modeling and optimization of magnetically coupled resonant wireless power transfer system with varying spatial scales," *IEEE Trans. Power Electron.*, vol. 32, no. 4, pp. 3240–3250, Apr. 2017.

Zhihao Wei was born in Shandong, China, in 1990. He received the B.S. and M.S. degrees in electrical engineering from the Qingdao University, Qingdao, China, in 2015 and 2018, respectively, and the Ph.D. degree in power electronics and power drives from the South China University of Technology, Guangzhou, China, in 2022.

He is currently a Lecturer with the School of Electrical Engineering, Qingdao University, Qingdao, China. His research interests include wireless power transfer technology and fractional-order system.

Bo Zhang (Fellow, IEEE) was born in Shanghai, China, in 1962. He received the B.S. degree in electrical engineering from the Zhejiang University, Hangzhou, China, in 1982, the M.S. degree in power electronics from the Southwest Jiaotong University, Chengdu, China, in 1988, and the Ph.D. degree in power electronics from the Nanjing University of Aeronautics and Astronautics, Nanjing, China, in 1994.

He is currently a Professor with the School of Electric Power, South China University of Technology, Guangzhou, China. He has authored or coauthored more than 450 papers, held 102 patents, and 8 monographs. His research interests include nonlinear analysis and control of power electronics, wireless power transfer technology, and ac drives.

Shan Lin received the B.S. degrees in electrical engineering and automation from the East China Jiaotong University, Nanchang, China, in 1993.

She is currently the Deputy Chief Engineer with the Guangzhou Metro Design and Research Institute Company, Ltd., Guangzhou, China, and also professor level Senior Engineer, registered Electrical Engineer, and registered Consulting Engineer. Her research interests include design and research of power supply, electrical, and intelligent system engineering.

Chunfang Wang (Member, IEEE) received the B.S. degrees in automatic testing technology from the Northeast Heavy Machinery College, Qiqihar, China, in 1984, the M.S. degree in power electronics and power drives from the Tsinghua University, Beijing, China, in 1993, and the Ph.D. degree in electrical engineering from the Xi'an Jiaotong University, Xi'an, China, in 2010, respectively.

From 1984 to 1990, he was a Research Assistant with Taiyuan Heavy Machinery College. Since 1993, he has been a Lecturer with the Department of Electrical Engineering, Qingdao University, Qingdao, China. He is currently a Full Professor with Qingdao University. His research interests include wireless power transfer technologies, electromagnetic and thermal field simulation of inductor devices, and small and medium-sized photovoltaic converters.